Characterization of the transverse profile of the PITZ photocathode laser

MASTERARBEIT

zur Erlangung des akademischen Grades
Master of Science
(M. Sc.)
im Fach Physik

eingereicht an der
Mathematisch-Naturwissenschaftlichen Fakultät I
Institut für Physik
Humboldt-Universität zu Berlin

von
Roman Martin
geboren am 18.04.1987 in Wriezen

Betreuung:

1. *Dr. habil. Christoph Janowitz*
2. *Prof. Dr. Thomas Lohse*

eingereicht am: *29. März 2013*   überarbeitete Version

Abstract

At the Photo Injector Test facility in Zeuthen (PITZ), electron sources are developed, that meet the high demands of modern scientific light sources like Free Electron Lasers (FEL). Here, the transverse emittance is a key parameter. The transverse emittance at the time of emission acts as a lower limit and is decisively determined by the intensity distribution of the cathode drive laser.

In this work, an algorithm for the characterization of the transverse intensity distribution of the PITZ cathode drive laser is developed. Various methods for automatically locating the laser spot and defining an Area of Interest (AOI) are compared. With this, a number of parameters for the characterization of the intensity distribution are presented and discussed. Among those are statistical quantities like the spatial correlation as well as various options for Fourier and Fourier-Bessel transforms.

Zusammenfassung

Am Photoinjektor-Teststand in Zeuthen (PITZ) werden Elektronenquellen entwickelt, die den hohen Ansprüchen moderner Forschungslichtquellen, wie Freie-Elektronen-Laser (FEL), genügen. Dabei ist die transversale Emittanz ein Schlüsselparameter. Die transversale Emittanz der Elektronenpakete unmittelbar nach der Emission stellt eine untere Schranke dar und wird maßgeblich durch die Intensitätsverteilung des Kathodenlasers bestimmt.

Im Rahmen dieser Arbeit wird ein Algorithmus zu Charakterisierung der transversalen Intensitätsverteilung des PITZ-Kathodenlasers entwickelt. Verschiedene Methoden zum automatischen Lokalisieren des Laserpunktes und zur Definition einer Area of Interest (AOI) werden verglichen. Darauf aufbauend wird eine Reihe von Parametern zur Charakterisierung der Intensitätsverteilung vorgestellt und diskutiert, darunter statistische Größen wie die räumliche Korrelation sowie verschiedene Möglichkeiten der Fourier- und Fourier-Bessel-Transformation.

Contents

List of Figures

Chapter 1

Introduction

Free electron lasers (FELs) play a more and more important role in photon science. Their applications range from condensed matter and surface physics to chemical and biological studies. The advantages of FELs over classical photon sources like synchrotrons are much higher pulse intensities with femtosecond short pulses of coherent radiation. Unlike conventional lasers, no active medium is needed for lasing. Instead, the radiation is produced by relativistic electrons, which not only allows for tunable photon wavelengths, but also wavelengths in the far UV and even the X-ray spectrum, which would destroy conventional laser mediums. However, operating in those regimes puts great challenges on the electron beam production.

Current and next generation FELs operating in the X-ray regime require high brightness electron beams [1]. This is achieved by producing high peak currents while keeping the transverse emittance low. A promising approach to accomplish this are photo injectors, where electrons are emitted from a cathode using a laser. At the Photo Injector Test facility in Zeuthen (PITZ), photo injectors for the existing FLASH and upcoming XFEL projects are developed, optimized and characterized, with an emphasis on emittance reduction.

The emittance is defined as the volume of a particle distribution in the 6D phase space $[x, y, z, p_x, p_y, p_z]$. With z chosen to be the beam axis, the transverse emittance is the particle volume in the 4D space $[x, y, p_x, p_y]$. The normalized transverse rms emittance of a distribution of particles is defined as

$$\epsilon_x = \beta\gamma\sqrt{\sigma_x^2\sigma_{x'}^2 - \text{cov}^2(x, x')} \tag{1.1}$$

and ϵ_y accordingly, with $\beta = v/c$ the ratio of particle speed and speed of light and γ the relativistic factor. x is the transverse offset from the beam axis of the individual particles and $x' = p_x/p_z$ is the ratio of the particle momentums perpendicular to the beam axis p_x and along the beam axis p_z. The factor $\beta\gamma$ ensures that ϵ is invariant under acceleration along z. σ_x and $\sigma_{x'}$ are the standard deviations of the mentioned parameters. In the following, "emittance" will refer to this normalized transverse rms emittance definition.

There are three main contributors to the emittance of an electron beam: the thermal emittance ϵ_{th}, which is the emittance of the electron bunch right after emission, and the emittance growth due to space charge forces ϵ_{sc} and RF defocusing ϵ_{RF} [2]. Assuming these contributors are independent, the total transverse emittance can be approximated by

$$\epsilon \approx \sqrt{\epsilon_{th}^2 + \epsilon_{sc}^2 + \epsilon_{RF}^2} \tag{1.2}$$

[3]. Since the emittance is only growing, the thermal emittance sets a lower limit to the total beam emittance, which makes it one of the key parameters in emittance optimization.

At the cathode surface, x and x' are uncorrelated, so the thermal emittance can be described by

$$\epsilon_{th,x} = \frac{1}{m_e c} \sigma_x \sigma_p \tag{1.3}$$

since $\beta\gamma = \frac{p}{m_e c}$ and $\sigma_{x'} = \frac{\sigma_p}{p}$ with σ_p the transverse rms momentum. In a simple model, electrons are emitted isotropically into a half-sphere in the vacuum [4]. The momentum distribution of mono-energetic particles calculated from this model is a function of the electron affinity, band gap energy and final state energy of the electron excitation, with the latter being dependent on the band structure of the cathode material and the wavelength of the cathode drive laser alone [5]. This means, once cathode material and laser wavelength are chosen, little can be done to tune the momentum distribution. Thereby, the thermal emittance is essentially determined by the rms laser spot size σ_x. Unfortunately, σ_x cannot be reduced to any desired value, because the smaller the spot size, the higher is the space charge density and thus the space charge forces which, in turn, increase the emittance. Thus, choosing σ_x must always be a compromise between thermal emittance and space charge induced emittance growth. Here it emerged, that for a given σ_x, the emittance growth is lowest, if the charge is distributed homogeneously, i.e. the transverse charge density distribution has a flat-top profile and the space charge forces are linear [6].

In the past, simulations where conducted, to estimate the impact of charge inhomogeneities at the cathode surface [7, 8, 9, 10]. In these simulations, initial flat-top distributions where modulated with sine and cosine functions described by the formulas

$$q = q_0 \cdot [1 + d \cos(k_n x)] \cdot [1 + d \cos(k_n y)] \qquad \text{and} \tag{1.4}$$
$$q = q_0 \cdot [1 + d \sin(k_n x)] \cdot [1 + d \sin(k_n y)] \tag{1.5}$$

with $x^2 + y^2 < R$ and $k_n = \frac{2\pi n}{R}$ for $n = 0.5...4$. All these studies came to similar results. While it is obvious, that the emittance growth is larger for larger values of d (with respect to q_0), it is also highly dependent on n. The results have shown, that inhomogeneities with high spatial frequencies n (i.e. small scale inhomogeneities) have a lower emittance growth compared to the ideal flat-top, than low frequency, large scale distributions, despite having the same modulation depth d. This is due to a stronger distortion of the beam shape for the low frequency distributions, while the high frequency distributions show a partial compensation of the inhomogeneities along the drift [7,8]. Some simulations also suggested, that charge distributions with the center of gravity different from the geometric center of the bunch ("asymmetric" distributions) have the severest impact on the emittance [10]. Simulations with radially symmetric distributions also showed large emittance increase for charge density maxima located off-center, while for distributions with a single maximum at the center, the emittance decreased to a certain degree. In the later case, non-linearities in the space charge forces within the bunch, that normally increase the emittance, are compensated by the smaller rms size of the distribution. However, most of the studies were exemplary and conducted for unrealistic charge distributions.

To allow for more detailed studies with more realistic conditions, this work aims to quantify characteristics of the actual charge distributions produced in the PITZ gun. The actual charge distribution is the product of the intensity distribution of the cathode drive laser and the quantum efficiency distribution of the cathode material. Unfortunately, no high resolution studies of the quantum efficiency distribution exist. For this reason, only the intensity distribution of the laser will be used as a measure of the charge distribution.

Chapter 2

The Photo Injector Test facility in Zeuthen (PITZ)

2.1 The photoinjector beamline

At PITZ, the electrons are generated by photoemission from a cathode illuminated by a pulsed UV drive laser of 457.5 nm wavelength. The cathode is Cs_2Te evaporated onto a molybdenum plug and has a thickness of $\approx$ 20 nm [4]. Since Cs_2Te is a semiconductor, it has a high Quantum efficiency of about 10% at the used laser wavelength [5, 11], which makes it a very efficient electron source. The cathode must be kept under ultra high vacuum conditions of 10^{-10} mbar to avoid poisoning by oxygen and carbon dioxide.

The PITZ gun is a normal conducting 1.6 cell L-band copper cavity operating at 1.3 GHz (Fig. 2.1). The RF power is provided by a 10 MW klystron and fed into the gun by a coaxial coupler. The maximum field gradient is $\approx$ 60 MV/m. Electrons leaving the gun cavity can reach energies of up to 6.7 MeV. The cathode is located in the half cell to allow for an efficient acceleration of the emitted electrons. Two solenoid are located around the gun: the main solenoid acts as a focusing lens and compensates emittance growth due to space charge forces. The bucking solenoid is compensating the magnetic field of the main solenoid at the cathode plane to avoid emittance growth induced by a residual angular momentum of the emitted electrons [12].

The complete PITZ setup (version PITZ 2.0) is shown in Fig. 2.2. Three dispersive sections, each made up of a dipole and a subsequent screen station, allow for momentum distribution measurements. Bunch length and longitudinal phase space measurements can be conducted at stations equipped with Cherenkov radiators and a streak camera. The booster cavity, a 9 cell copper cavity, accelerates the bunches to a maximum energy of $\approx$ 25 MeV. After the booster, two EMittance Measurement SYstems (EMSY) are installed. They can measure the emittance via slit scan method separately in x and y. Applying off-crest acceleration in the booster, an energy chirp along the bunch can be produced, such that the longitudinal momentum of the electrons can be correlated with their position in the bunch. This way, the bunch can be cut into longitudinal slices by the 180° dipole after EMSY2 and a slit. The horizontal emittance of the slices can be measured by the slit scan or the quadrupole scan method. The phase space tomography module (PST) located 11.5 m downstream the cathode enables to measure the beam emittance using the tomographic reconstruction [13]. Unlike the EMSY stations, the PST module can
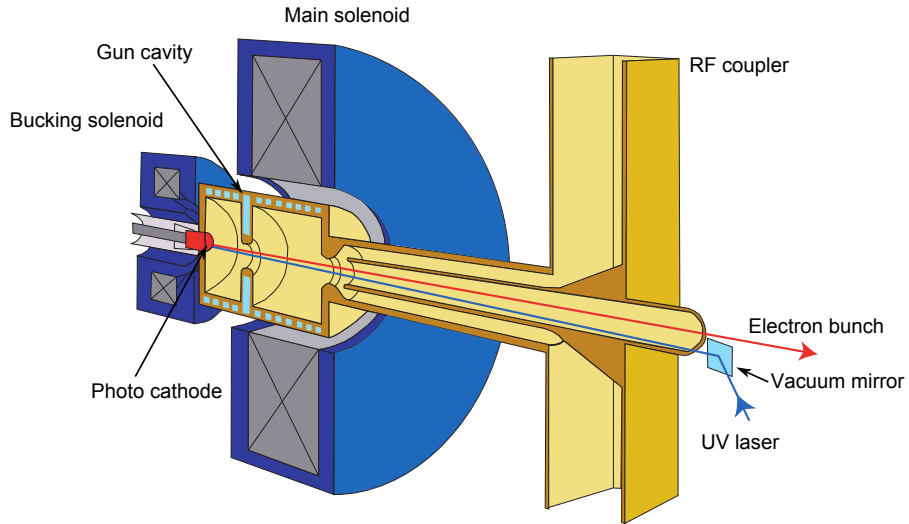
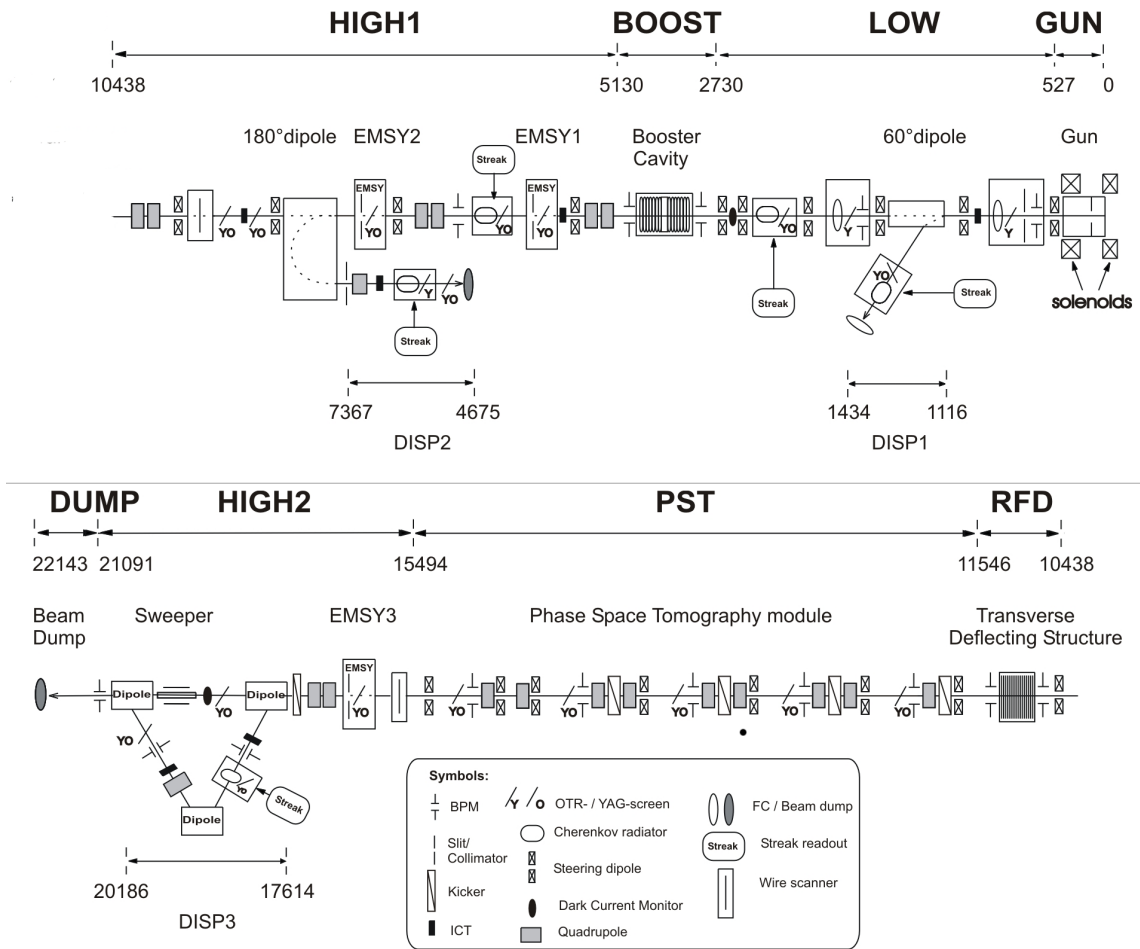**Figure 2.1:** Electron gun setup at PITZ

Figure 2.2: Schematic layout of the PITZ 2.0 beam line

measure x- and y-emittance simultaneously and with a better resolution. The transverse deflecting structure, a 3 GHz RF cavity located before the PST, will, together with a fast kicker magnet, enable slice emittance measurements and slice momentum distribution measurements of single bunches at the last dispersive section (DISP3). After the third dispersive section, the beam is brought back into the original beam line and sent to the beam dump.

2.2   The PITZ Laser system

The PITZ photocathode laser was developed at the Max-Born-Institute, Berlin [14]. It consists of a Yb:YAG laser oscillator with several Yb:YAG amplification stages lasing at 1030 nm wavelength, producing micro pulses at 1 MHz repetition rate. The pulses are organized in pulse trains of up to 800 single pulses with 10 Hz repetition rate (Fig. 2.3). The Gaussian temporal shape of the single pulses is transformed into a flat-top pulse by a pulse shaper comprising 13 birefringent crystals. The flat-top pulses have a FWHM duration of up to 22 ps with rise and fall times of ≈ 2 ps. When entering a birefringent crystal in the pulse shaper, the Gaussian pulse is split into two pulses with perpendicular polarizations. Since both pulses have different refractive indices, they propagate at different speeds, resulting in a temporal separation determined by the thickness of the crystal. By successively repeating this step, multiple Gaussian profiles are overlayed to form a flat-top profile [14].

After the amplification stages the infrared light is converted to the ultraviolet by two successive frequency conversion crystals (LBO and BBO), each dividing the incoming wavelength by two to the output wavelength of 257.5 nm. The intensity of the laser can be tuned via a rotatable half-wave plate followed by a birefringent crystal used as polarizer. The maximum pulse energy of the UV pulse is ≈ 10 μJ. The temporal profile of the pulse is monitored in the Optical Sampling System (OSS) by using a cross-correlation method scanning the UV pulse with the original IR pulses. The resolution of this method is about 2 ps.

2.3   Laser beam line and diagnostics

From the laser room, the beam is transmitted over a distance of 13.0 m into the accelerator tunnel, magnifying and imaging it on the Beam Shaping Aperture (BSA). The BSA - initially consisting of a set of exchangeable plates with holes of fixed diameter but later replaced with a remotely controlled iris diaphragm - cuts out the central part of the transverse distribution. Since the original transverse distribution is shaped Gaussian like, the beam needs to be magnified such that the cut-out part is almost a flat-top distribution. However, there needs to be a compromise with the lost energy at the BSA. By changing the diameter of the BSA the laser power at the
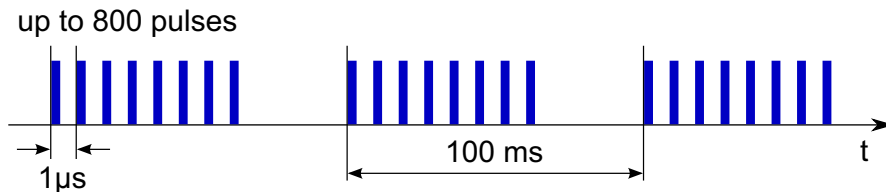

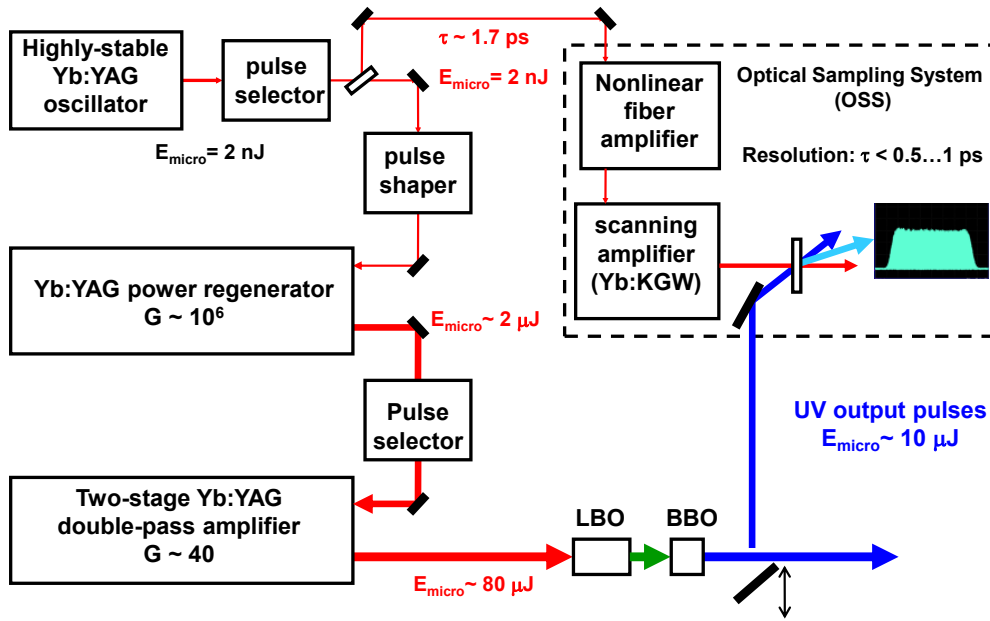**Figure 2.3:** Time structure of the cathode laser

Figure 2.4: Schematic view of the PITZ Laser system. Illustration by I. Will (MBI)

photocathode - and thereby the charge extracted from the photocathode - can be controlled. Depending on the desired charge, the BSA diameter is usually between 100 μm and 1500 μm.

After the BSA a setup of four lenses is imaging the beam onto the cathode with unit magnification over a distance of 6.9 m. Fig. 2.5 shows a schematic view of the laser diagnostics assembly. Shortly after the lens system, a crystal wedge reflects a small percentage of the laser intensity towards the PCO camera, which contains a CCD chip preceded by a photocathode, multichannel plate (MCP) and a phosphor screen. With the accelerating voltage between photocathode and MCP acting as a shutter, the shutter time is much smaller than the usual readout time of CCD chips. This makes measurements of single micro pulses possible, e.g. position and position jitter, beam size and beam size jitter, as well as energy stability. The position of the laser spot on the photocathode and the incident angle can be changed by two mirrors M5 and M6. A quartz wedge permanently reflects a part of the laser light towards various diagnostics, including a quadrant diode (QD) to measure the beam position stability, photo multiplier tubes (PMT), a photo diode (PD) for laser pulse energy measurements and a CCD camera. The CCD camera has the same optical path length as the photocathode and therefore measures the transverse intensity distribution at a plane equivalent to the cathode plane. Hence it is named Virtual Cathode (VC1). Since the front and back side of the quartz wedge have reflectivities of only $\approx$ 4 %, VC1 can only be used in the high intensity regime or for a large number of micro pulses. Another Virtual Cathode (VC2) can be used on demand by moving a mirror into the beam line, and is used in the low intensity regime [10].

All beam images used in this work where taken from VC2, a CCD camera of type JAI Pulnix TM1405-GE OP21-1UV with a resolution of 1392 x 1040 pixels and a pixel size of 4.65 μm x 4.65 μm. The CCD camera at VC1, type JAI M10 SX, does
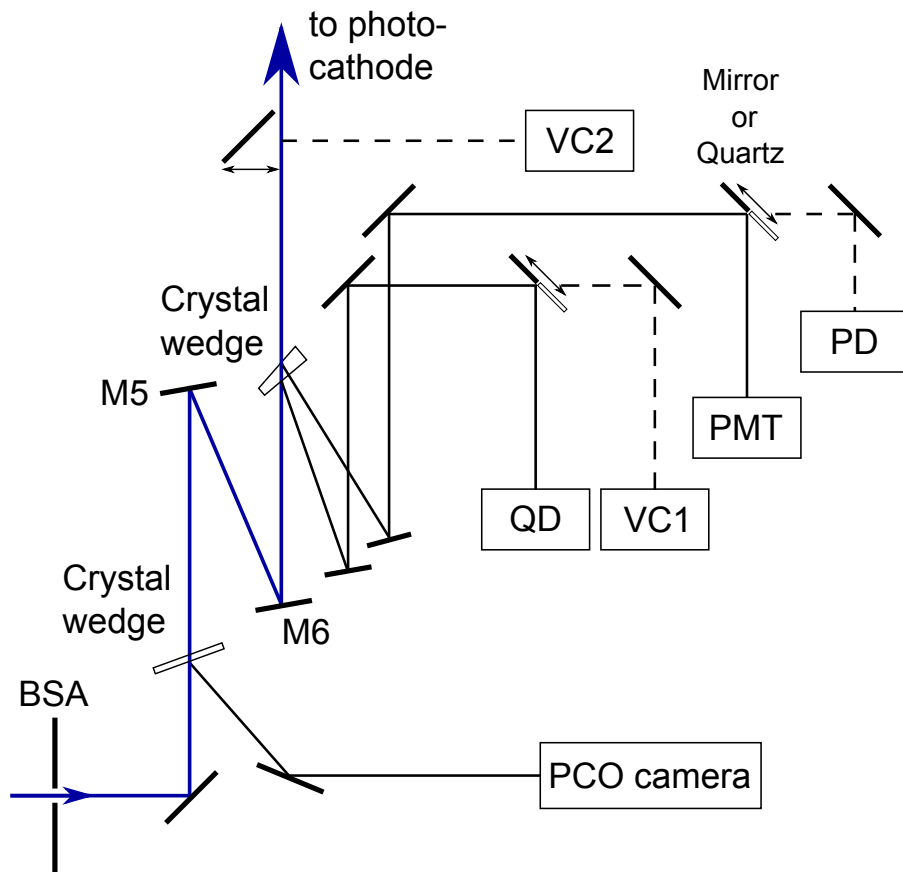
Figure 2.5: Schematic view of the assembly of the laser diagnostics after the BSA.

not only have a lower resolution and larger pixel size, but it also showed blooming issues even with the relatively low intensities reflected by the quartz wedge, and therefore was not used.

The cameras are synchronized with the timing system of the photo injector and are operated via a specially designed, TINE based video system [15]. Since the VC2 camera has a read-out rate of only 30 Hz, only single pulses were used, in order to avoid overexposure and blooming. For statistical reasons, one measurement includes several individual images (usually 10, sometimes 20 or 30) of single pulses, each in a separate pulse train. Every image is saved separately. This procedure is repeated without sending the laser beam onto the virtual cathode for background subtraction.

The analysis in this work is done with MATLAB. The PITZ standard algorithm was used to convert the image files into MATLAB matrices: For the pixel values of the individual images, the mean was calculated

$$v(i,j) = \frac{1}{N_I} \sum_n^{N_I} v_n(i,j) \tag{2.1}$$

with $v_n(i,j)$ being the pixel value at (i,j) of the nth individual image and N_I the number of images. For every pixel of the background image, the highest of the pixel values of the individual background images was chosen:

$$b(i,j) = \max\left(b_1(i,j), b_2(i,j)...b_{N_I}(i,j)\right) \tag{2.2}$$

with $b_n(i,j)$ the pixel value at (i,j) of the nth individual background image. The
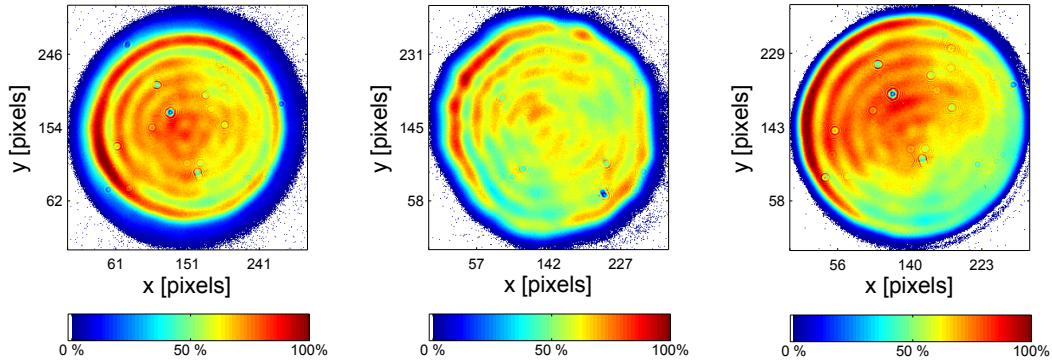
Figure 2.6: Typical imaging errors: diffraction patterns can be seen in all three images, as well as dust. The laser spot in the center shows an irregular edge due to the iris opening not being perfectly round, for the right spot the BSA was not illuminated homogeneously. All laser images in this work will use the same color scale, so it will not be shown in further illustrations.

final image was then calculated as

$$a(i,j) = v(i,j) - b(i,j) \tag{2.3}$$

with subsequently all pixel values < 0 being set to zero. This procedure makes sure that any systematical background is eliminated but on the other hand cannot deal with background noise. In fact it is likely that the statistical noise of the non-zero pixels is even larger since the zeroing does not compensate the subtraction of a random value here. However it will be shown that background noise and statistical uncertainties of the pixel values are a minor effect.

2.4 Analysis of the transverse laser profile

Although the BSA cuts out a very small part of a very broad Gaussian like distribution, the resulting image on the virtual cathode is everything but smooth. Typical imaging errors can be seen in Fig. 2.6.

- The right laser spot is highly asymmetric because the BSA is not illuminated homogeneously. This problem occurs mainly for large BSA diameters when no homogeneous, large region can be found in the original intensity distribution.

- The laser spot in the center shows irregular edges, typical for the use of a BSA where the blades of the iris do not form a perfectly round aperture.

- Due to constructional restrictions the cameras are pointing upwards, allowing deposition of dust. The same applies for other optical elements such as mirrors and lenses. The dust can be seen as more or less prominent dot, partly just a diffraction pattern (small grains) and partly as a completely unilluminated area (larger grains). These measurement artifacts do not necessarily occur in the intensity distribution at the photocathode.

However, the most prominent structures on the laser spots are the concentric diffraction patterns. With perfect imaging, these patterns would not appear, since the lens
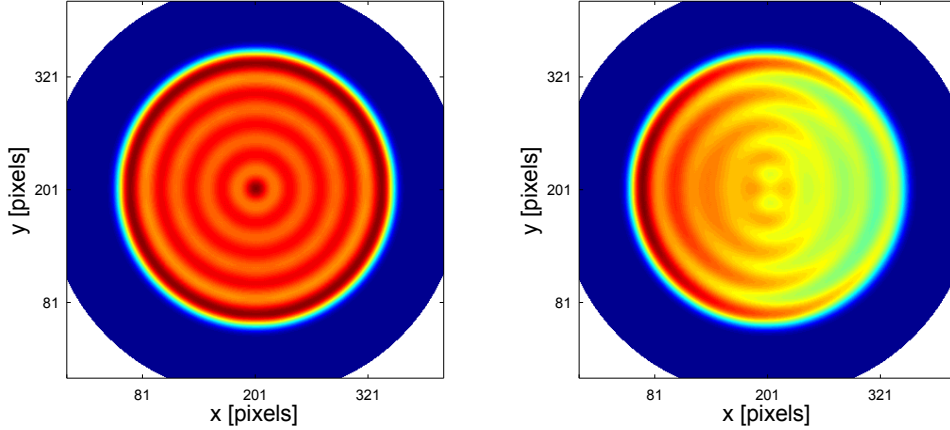
9

Figure 2.7: Calculated diffraction patterns with homogeneously illuminated BSA and aperture in the center (left), with linear intensity gradient in x and aperture shifted off-center in y (right).

system would image the intensity distribution at the BSA on the camera. Unfortunately, the imaging is restricted by the aperture size of the optical components of the laser beam line. This can be explained with Fourier optics: after the BSA, the beam diverges due to diffraction. The focusing of the lens system simply reverts this process. Mathematically, this can be described as two successive Fourier transforms that, of course, should reproduce the original intensity distribution. Unfortunately, the aperture size of the laser optics is only 3 inches at some points of the beam line and therefore cuts outer parts of the divergent beam [16].

The effect of this can be demonstrated in a simple example, where the limiting aperture is at the Fourier plane (i.e. the plane where the intensity distribution of the diffracted beam is exactly the Fourier transform of the distribution at the BSA). Two calculated beam images can are shown in Fig. 2.7. In both cases a circular initial distribution was Fourier transformed. The initial distribution on the left was a perfect flat-top while on the right, a linear intensity gradient was used. On the left side, the resulting image was cut by a centric, round aperture, on the right side, a rectangular, off-center aperture was applied. Both images where then again Fourier transformed, resulting in the shown distributions. The calculated images describe some measured distributions quite well but must be considered as a simplified model since the limiting aperture is not at the Fourier plane, so the cut distribution is not exactly the Fourier transform. In fact, the intensity is cut at several locations. While the Fourier plane is in the middle of the four lens system, most intensity is cut by the third and fourth lens. The number of rings on the flat-top profile as well as their intensity depend on the number of diffraction orders cut by the aperture. More transmitted diffraction orders result in more rings of smaller intensity.

It should be noted, that recent tracking simulations of the laser beam have shown, that the vacuum mirror (see Fig. 2.1) is also restricting the beam diameter [17]. Since this limiting aperture is located behind the mirrors to the virtual cathodes, its impact cannot be seen in the images delivered by the VC cameras. The simulated effects are noticeable at BSA sizes smaller than $500\mu m$, but only get severe for BSA's below $100\mu m$. Since the laser spots lose their flat-top character for BSA sizes below $400\mu m$ due to the 3 inch optics anyway, this effect can be neglected.
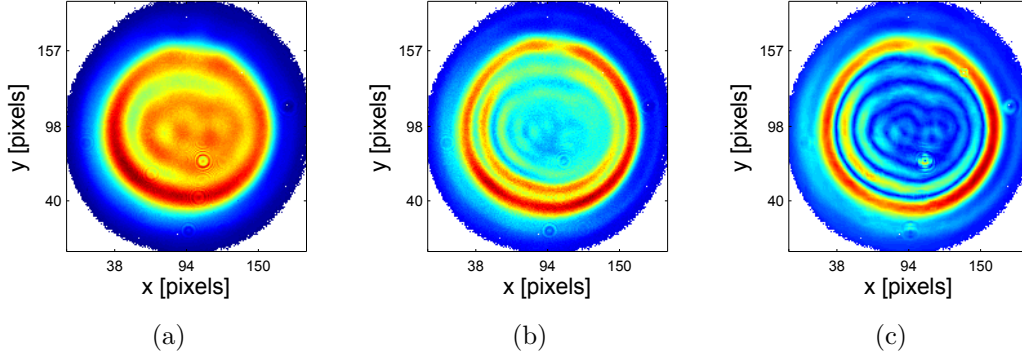
Figure 2.8: From left to right: original laser spot, rms map and gradient map. The color scale of the gradient map was chosen arbitrarily for a better comparison with the rms map.

The fact that every measurement comprises 10 or more images makes it possible to do a statistical analysis of the resulting image which is simply the pixelwise mean of the single images (ignoring the background subtraction). By calculating the standard deviation of any pixel, i.e.

$$\sigma_v(i,j) = \sqrt{\frac{1}{N_I} \sum_n^{N_I} \left(v_n(i,j) - v(i,j) \right)^2} \tag{2.4}$$

with the parameters as in equation 2.1, the resulting images (in the following called rms maps) represent the distributions of variance. For most kinds of statistical distribution of the pixel values $v_n(i,j)$ (e.g. Poisson distribution, for CCDs probably percentage error), a larger pixel value implies a larger standard deviation. However, when comparing the laser spots with the rms maps this is not the dominant factor, as can be seen for an exemplary spot in Fig. 2.8(a) and 2.8(b). The area around the center of the laser spot has a relatively high intensity but the rms is significantly lower than at the edges with similar intensity. Also, overlaying both images reveals that the position of the rings of higher rms do not match the diffraction pattern intensity of the laser spot. Instead it seems to match the flanks. To verify this, the numerical gradient $\sqrt{\left(\frac{\partial I}{\partial x}\right)^2 + \left(\frac{\partial I}{\partial y}\right)^2}$ was calculated for every pixel in the laser spot (after smoothing). The resulting gradient map can be seen in Fig. 2.8(c). Overlaying with the rms map shows a good match. Apparently a high rms comes with a high gradient in intensity. This can be explained by the laser position jitter, as seen in Fig. 2.9.

For a jitter magnitude significantly smaller than the described feature, the change in the pixel values (according to the length of the blue arrows) is much smaller at the point of highest intensity than on the flanks of the feature.

Measurements have shown that the magnitude of laser jitter significantly increases in the vertical section of the beam line (the laser shaft) located between the laser room and the tunnel, while it remains almost constant after the BSA [18]. It was therefore concluded that the laser jitter is mainly caused by mechanical vibrations of the mirrors and airflow in the shaft. The transverse jitter of the laser beam before the BSA can be neglected since this would primarily change the intensity of the diffraction pattern on the cathode but not its position. Therefore the jitter that is seen on the rms maps comprises the resulting angular jitter and the relative transverse position jitter between BSA and cathode (or virtual cathode).
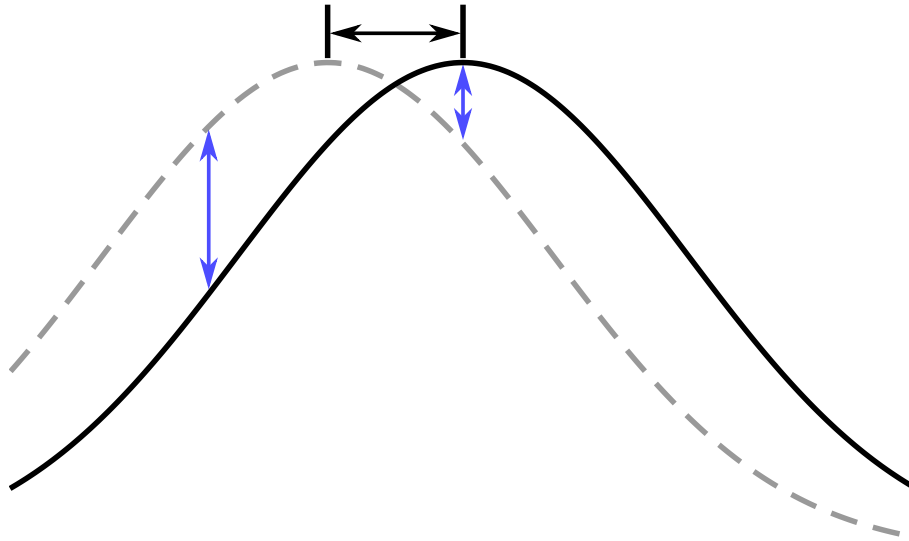
Figure 2.9: Laser jitter causing a high rms at the flanks of the feature and a low rms on top.
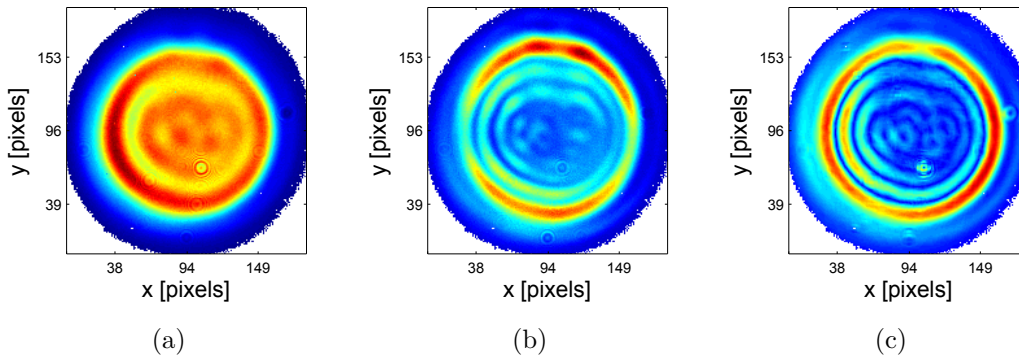

(a) (b) (c)

Figure 2.10: From left to right: original laser spot, rms map and gradient map. Note how structures of the rms map and gradient map correspond in position but not in height. In this case the laser beam jitter occurred mainly in along the y axis, therefore the high gradients on the right and left side of the laser spot contribute only marginally to the rms.

It becomes apparent that the structures on the rms map and gradient map match in position but not necessarily in relative height. This is probably caused by the direction of the beam jitter. The gradient map is calculated by Pythagorean addition of the gradients in x an y direction and can therefore be considered the greatest rate of increase at this location. If the beam jitter has a different (mean) direction than this gradient, the latter will not contribute to the rms to its full extent. An extreme can be seen in Fig. 2.10, where the beam jitter mainly occurred along the y axis. The rms values on the right and left side are rather small, because the gradient direction is perpendicular to the main direction of the jitter.

It should be noted that these findings apply only to the images taken with the CCD camera. For single pulses of ≈ 20 ps length, the mirrors can be assumed to be static since the period of mechanical oscillations can be assumed to be on a much larger time scale. On the other hand, most measurements at PITZ use more than one pulse and take much more time than seconds, so the rms maps might describe the uncertainties quite well.

In addition to the assumed percentage error, CCD cameras have intrinsic noise. Due to local heating of the chip, the measured intensity becomes higher than the real intensity. Since the change depends on the intensity, this systematic error cannot be eliminated with the background subtraction. Neither can it be estimated by statistical considerations, so no corrections can be applied.

Chapter 3

The Area of Interest

To analyze the laser spots it should first be considered, which parts of the distribution should be included in the analysis. As can be seen in exemplary laser images, the shape of the distribution is far from being flat-top. Not only the to-be analyzed modulations of the top play a role here. Also the flanks are not sharp edges as expected from a flat-top, but are rather broad. This will lead to problems when calculating characterization parameters like a standard deviation: including the flanks will bias the calculation of the mean towards lower values. Depending on up to which point the flanks are included, the mean will be more or less significantly lower than the 'flat-top' part of the distribution, decreasing the significance of the resulting standard deviation (especially since the deviation at the flanks will still be very high). If, on the other hand, an rms error is applied instead of a standard deviation (i.e. not the deviation from the mean but from an arbitrary function) the flanks will be posing a problem as well. It is very unlikely that a function is found, that describes the flanks perfectly. Due to flanks usually being very steep, the deviations occurring here will be very large and will thereby strongly affect the rms value. Of course the flanks are non flat-top features of the distributions and therefore need to be characterized. Nevertheless the influence on the rms largely depends on the function describing the flanks and is therefore a poor measure for this purpose. Furthermore, modulations on the flanks are likely to have a much smaller influence on the emittance than the shape of the flanks itself.

For these reasons it is rational to analyze flanks and flat-top part separately. To do this, an area of interest (AOI) needs to be defined. Also it is imperative to find this AOI automatically. If human interaction is necessary for AOI definition (e.g. defining the center/size of the spot or of the AOI), results for the characterization parameters depending on the AOI will not be reproducible, thereby reducing their sensitivity and significance.

For the following studies on AOI definition, a set of 280 laser images taken between 23 March 2011 and 1 February 2012 was used.

3.1 One-dimensional approach

In a first approach, a procedure was tested that only uses one-dimensional arguments to find the AOI. To define the center and the borders, the matrix representing the
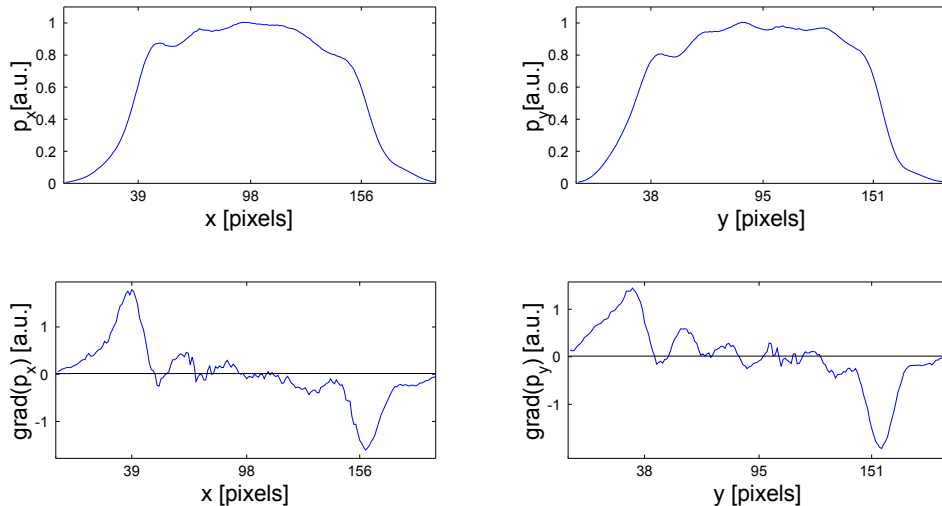
Figure 3.1: Projections of the laser spot in x and y and the corresponding gradients below. The gradients have a distinctive, more or less antisymmetric shape.

laser spot $a(i, j)$ was projected onto the x- and y-axis, respectively:

$$p_x(i) = \sum_j a(i, j) \tag{3.1}$$

$$p_y(j) = \sum_i a(i, j) \tag{3.2}$$

The gradient of these projections has a distinctive shape as illustrated in Fig. 3.1.

As an initial attempt, the x and y values with the highest and lowest gradients were used as the boundaries of the AOI. The coordinate of the center was assumed to be exactly at the middle between these boundaries. The halve of the distance between the boundaries was taken as the radius. This shows a first weakness of the one-dimensional approach: the radius obtained in x will not be the same as in y. There is no way to decide which radius should be used. Averaging both radii can be a solution.

In this first attempt, large grains of dust covering large areas of the CCD chip had notable influence on the projections and their gradients. For the spot in Fig. 3.2 the intensity drop is large and steep enough to, even in the projection, produce a gradient larger than the flank gradient. This fatally effected the deduced AOI, making the AOI definition unreliable. This issue was solved by smoothing the gradients with a smoothing window of ±5 pixels.

Another problem are rather broad gradient peaks, possibly with multiple local maxima. Here it is not clear, where to set the boundaries. Depending on where the absolute maximum of the peak is located, the AOI can be shifted significantly. Fig. 3.3 shows such a laser spot. Attempts have been made to solve this problem by fitting the gradients and using the extrema of the fit function. Several combinations of tailed distribution functions roughly resembling the gradient images have been tested. This usually comprised one function for the positive and one for the negative part. Combinations of two Weibull distributions, Giddings peak functions and log-normal distributions were tested. However, while the Weibull functions could not produce any fit results at all, the results for the other functions where not satisfying. Attempts with single, symmetric fit functions treating the gradients as a whole, instead of separating positive and negative part, failed for gradients as shown in

Figure 3.2: Laser spot with a blue circle marking the AOI (left), projection in x and corresponding gradient (right). Note how the center of the AOI is shifted due to the intensity drop caused by dust. In this case the radius obtained in y was applied.

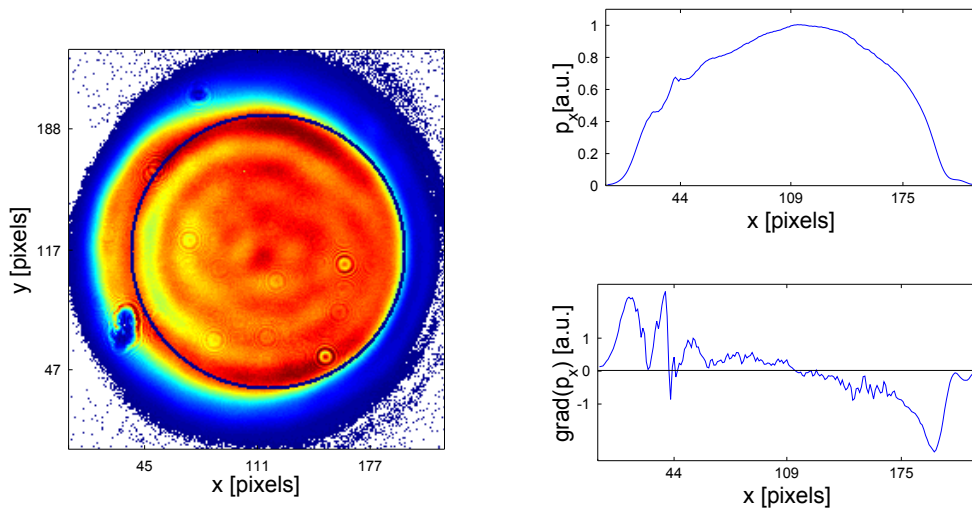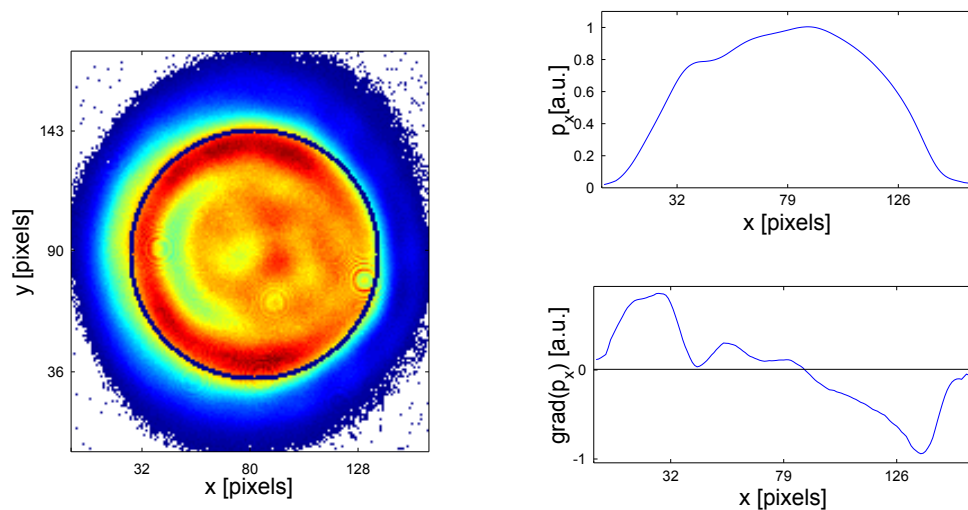**Figure 3.3:** Laser spot with a blue circle marking the AOI (left), smoothed projection in x and corresponding gradient (right). The rather broad left peak in the gradient diagram with its maximum on its right shifts the AOI notably to the right.
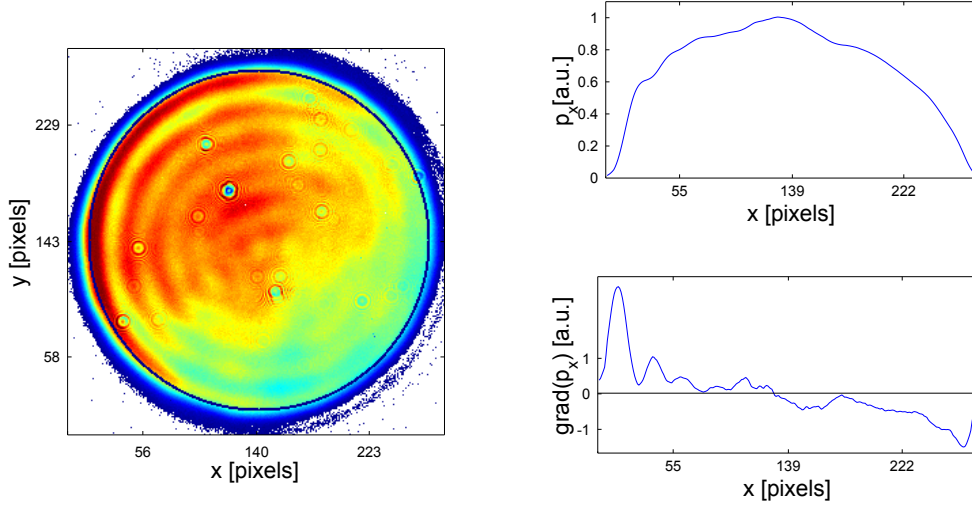
Figure 3.4: Gradient in x for a spot with remarkably asymmetric diffraction pattern. The asymmetry prevented fitting with a single, symmetric function.

Fig. 3.4, due to the significant asymmetry. All in all, fitting the gradients produced no reliable results.

Upon closer examination, the exact positions of the maximum gradients seem to be determined by the diffraction pattern. If the diffraction pattern is asymmetric, the obtained center and limits of the AOI will be shifted accordingly. This can be seen in Fig. 3.5. While the underlying intensity distribution is rather homogeneous, the diffraction pattern in the lower part of the laser spot is higher than in the upper part. The gradient shows none of the problems discussed above, but a cut through the laser spot along y axis reveals that the AOI is shifted upwards anyway.

This is undesirable since the inhomogeneities on the underlying, ideally flat-top distribution have to be analyzed. Therefore the AOI should be defined by this distribution and not by the inhomogeneities. Otherwise the AOI can change significantly with a change in the diffraction pattern, thereby possibly making the results incomparable although the underlying distribution has not changed at all. This obviously cannot be achieved by a simple one-dimensional approach. The lessons learned from this, call for an approach, where the underlying distribution is the major factor in defining the AOI. This can only be done in two dimensions, where no axes play a special role like x and y axis in the one-dimensional approach. A powerful tool that meets these requirements is the fitting of a given 2D function to the laser intensity distribution. This will be the subject of the following section. However, despite its shortcomings, the gradient method has proven to be reliable and fast enough to serve as an initial guess for the two-dimensional fitting.

Before the two-dimensional fitting is discussed, an even more simple approach must be ruled out. One can argue, that the AOI could simply be defined with a threshold. Pixels with a value above the threshold would be part of the AOI, pixel values below would be excluded from analysis. The problem with this method is the definition of the threshold. A simple percentage of the maximum pixel value must be ruled out since the diffraction pattern can attain values more than two times the height of the underlying distribution. Also the underlying distribution itself can be highly asymmetric, thereby excluding parts of it. Sometimes even the diffraction pattern of dust grains can determine the scaling of the intensity height with just a few pixels. Examples can be seen in Fig. 3.6. The threshold therefore would need to
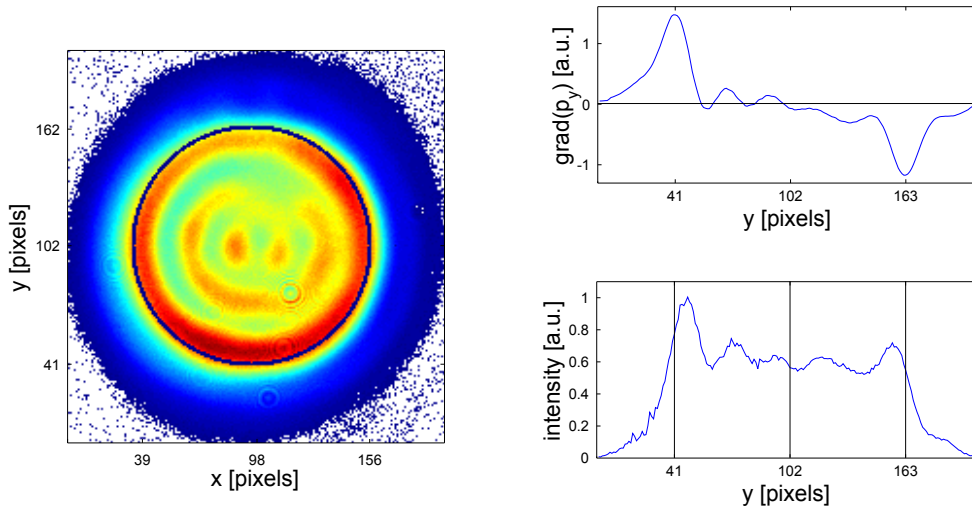
Figure 3.5: Laser spot with a blue circle marking the AOI (left), projection gradient in y and cut through the spot with center and AOI limits marked (right). Note how the limits are obviously determined by the diffraction pattern and not by the underlying intensity distribution. Since the inhomogeneity of the distribution has to be characterized, this is undesirable.
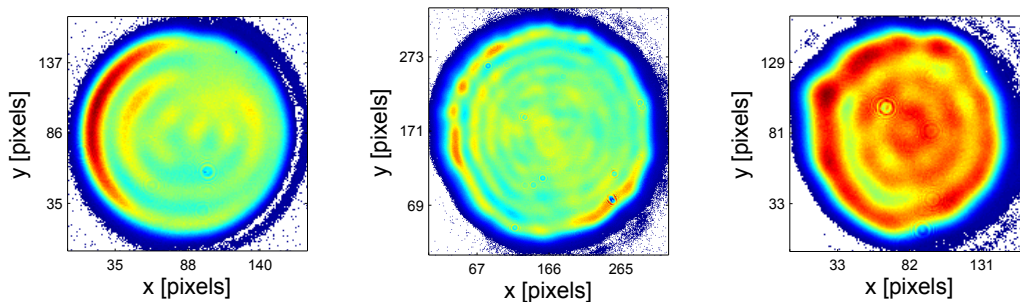
Figure 3.6: Laser spots with different ratios of underlying and maximum intensity. From left to right: high diffraction pattern on one side, dust causing immense intensities in few pixels around the covered area, relatively flat inhomogeneities. The differences can be deduced from the varying color scaling.

be low compared to the maximum. With this, the ratio of underlying distribution and diffraction pattern has a large impact on the extend to which the flanks are still part of the AOI. Relatively homogeneous laser spots would still include large parts of the flanks. If, on the other hand, the threshold is scaled on the basis of an average intensity, the area contributing to this average needs to be defined. An AOI begets an AOI, which just adds another iteration to the problem. All in all, a threshold is impractical and the results would vary widely concerning the exclusion of the flanks.

3.2 Two-dimensional fitting

With the one-dimensional approach producing unsatisfactory results, the two-dimensional approach aims to avoid the problems that occurred. As discussed above, this means the AOI must be determined mainly by the underlying intensity distribution

while the inhomogeneities have to play a minor role or no role at all. The best way to do this is by using a fit function that only describes a flat-top distribution.

The simplest fit function would be the ideal case, a flat-top function with the edges defined by the unit step function (or Heaviside step function):

$$f_{St}(r) = A \cdot H(r_0 - r) = A \cdot \begin{cases} 0: & r > r_0 \\ 1: & r \leq r_0 \end{cases} \tag{3.3}$$

with $r = \sqrt{(x - x_0)^2 + (y - y_0)^2}$, (x_0, y_0) the coordinate of the center and r_0 the radius of the flat-top distribution. This, however, has one major disadvantage. The actual laser spots do not have sharp edges but rather broad flanks. With f_{St} as a fit function, r_0 would be chosen to be approximately at the middle of the flanks. The original aim of the AOI, the exclusion of the flanks can not be achieved by using r_0 as the radius of the AOI. It is also impossible to reduce r_0 by the width of the flanks, since no information on the flanks is obtained. Therefore a fit function has to be found, that has variable flanks, preferably defined by a free fit parameter.

One possible candidate is the Fermi-edge like function

$$f_F(r) = \frac{A}{\exp \frac{r - r_0}{T} + 1} \tag{3.4}$$

The parameter A again just gives the height of the fit function, while T is a measure of the width of the flanks. There is no physical reason to use this kind of function, but it has a variable shape resembling the flanks of the laser spot. Also it is quite easy to estimate the width of the flanks with the standard approximation of $4T$. This can be deduced from the Taylor expansion of $f_F(r)$ around $r = r_0$:

$$f_F(r) = \frac{A}{2} - \frac{A}{4T} \cdot (r - r_0) + O\left((r - r_0)^2\right) \tag{3.5}$$

Since $f_F(r)$ can only have values between 0 and A, the linear approximation only works within an interval of $r - r_0 \in [-2T, 2T]$. With this approximation, the radius of the AOI was chosen to be $r_0 - 2T$ which crops large parts of the flanks.

For the fitting of the laser intensity distribution, the MATLAB function `lsq-curvefit` was used. This function applies the least squares method with the default algorithm being the `trust-region-reflective`-algorithm. In Fig. 3.7 one of the laser spots discussed above can be seen with the AOI determined by fitting with $f_F(r)$. The AOI is not shifted in y anymore, as it was with the one-dimensional approach. It does however look shifted in x. This is due to the flanks not having the same width on both sides. As a consequence, the diffraction pattern is not concentric with the AOI, on the right side larger parts are cut away than on the left. This problem cannot be solved without adding significant complexity to the fit function, which would also reduce its reliability.

Since elliptical laser spots have occurred in earlier setups, the shape of the AOI was changed from circular to elliptical. The elliptical shape was probably caused by reflections in the crystal wedges or by inhomogeneities in the conversion crystals caused by radiation damage. Unfortunately, no such spots could be provided, to be included in this work. To describe the ellipse, the implicit definition

$$\left(\frac{x - x_0}{\sigma_x}\right)^2 + \left(\frac{y - y_0}{\sigma_y}\right)^2 - \frac{2\sigma_{xy}}{\sigma_x^2 \sigma_y^2}(x - x_0)(y - y_0) = E(x, y) \tag{3.6}$$
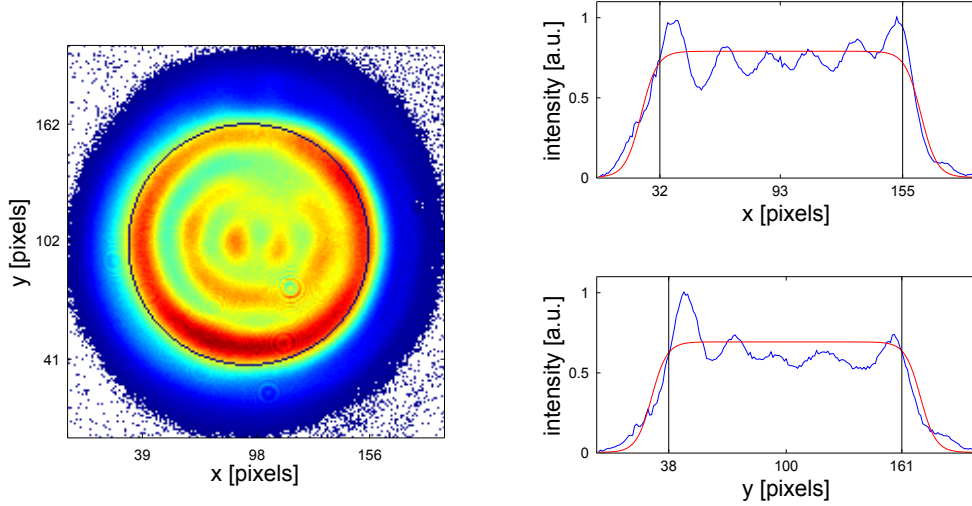
Figure 3.7: The same laser spots as in Fig. 3.5, this time with the AOI obtain by fitting (left), cuts along x and y axis through the center of the AOI (right). The fit result is plotted in red. Note how the position on the y axis is much better now. On the x axis however, the AOI seem to be shifted due to the flanks not being symmetric.
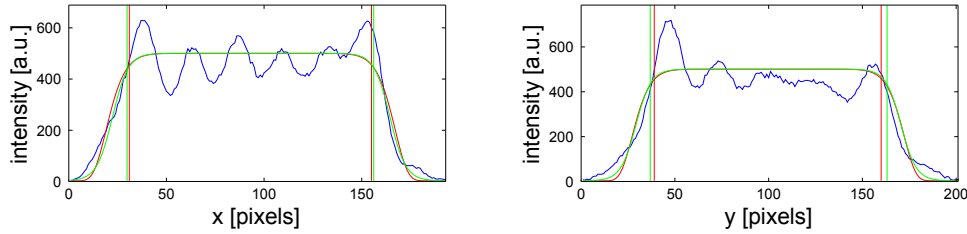

Figure 3.8: Cut through laser spot fitted with Fermi-edge like fit function (green) and Super-Gaussian fit function (red) with the edges of the AOIs marked accordingly. Both functions have similar results. Note that the Super-Gaussian is already elliptical.

with $E(x, y) = $ const. for a certain ellipse, was used, a definition that originates from statistics.

Furthermore, the fit function was replaced by a Super-Gaussian, a more typical approach to describe laser intensity distributions [19]. The elliptical Super-Gaussian is expressed by

$$f_{SG}(x, y) = A \cdot \exp\left(-\frac{1}{2\left(1 - \frac{\sigma_{xy}^2}{\sigma_x^2 \sigma_y^2}\right)} E^{\frac{G}{2}}\right) \tag{3.7}$$

with $G > 2$, which basically is a normal Gaussian with a higher exponent, i.e. steeper flanks. For $G \to \infty$ it will be a perfect flat-top. Since the broadness of the flanks of the Super-Gaussian cannot be estimated as easily as for $f_F(r)$, the AOI is defined as the area, where $f_{SG}(x, y)$ is greater than 90% of its maximum A. In Fig. 3.8 the fit results of Super-Gaussian and Fermi-edge function are compared. Both differ mainly in the flanks, which are excluded anyway. Also the AOIs are almost the same, although defined differently. Therefore switching to the Super-Gaussian poses no problems.

To further investigate the effects of asymmetric intensity distributions on the
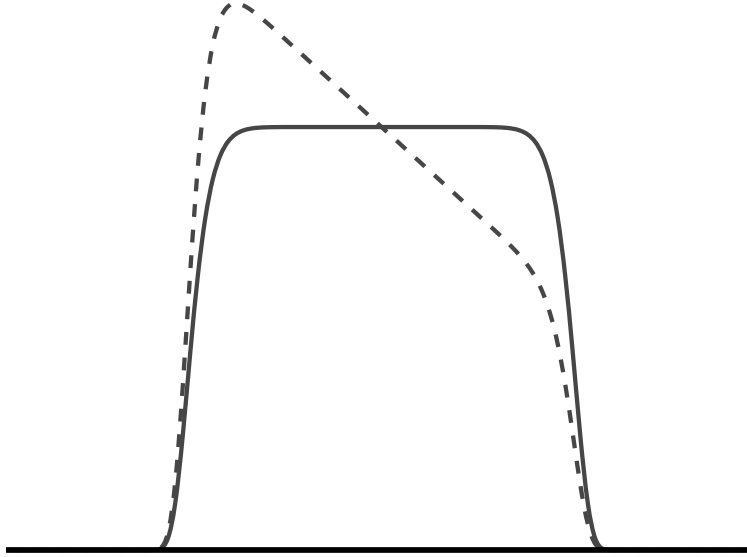
Figure 3.9: Super-Gaussian (solid line) and Super-Gaussian multiplied with plane (dashed line). Both Super-Gaussiant have the same center. Note how the flanks are affected by the plane. The fitting algorithm will compensate this by shifting the center. Since the AOI is defined only by the Super-Gaussian part, it will be shifted accordingly.

AOI, $f_{SG}(x, y)$ was multiplied with the plane

$$z = 1 + \alpha x + \beta y \tag{3.8}$$

with α and β as additional fit parameters. In the case of success, the absolute value of the gradient of the plane $\sqrt{\alpha^2 + \beta^2}$ could also be used to characterize the asymmetry. By multiplying this plane to the Super-Gaussian, instead of, for example, addition, the value of the resulting fit function far from the actual spot will still be almost zero, so the plane will pose no problem with the unilluminated parts of the image. The result of the fit will be asymmetric, so the previous definition of the AOI of 90% of the maximum or of A will not work, because it excludes the parts of the Super-Gaussian, that are lowered by the plane. Therefore the AOI was chosen to be the parts that are above 90% of the Super-Gaussian without the plane but with otherwise equal parameters.

The AOIs obtained with this fit function showed considerable differences to the previous AOIs. While few asymmetric laser spots had better AOIs, most of them were much worse, especially for spots with only the diffraction pattern being asymmetric. Fig. 3.9 gives a possible explanation: The plane multiplied on top of the Super-Gaussian manipulated the flat-top region of the original distribution, but it also affected the flanks. To compensate this, the underlying Super-Gaussian was shifted towards the direction of the plane's gradient to match the flanks again. The AOI however, was calculated with the now shifted Super-Gaussian part only and therefore was shifted too.

To investigate this, the angle of the plane's gradient direction $\begin{pmatrix} \alpha \\ \beta \end{pmatrix}$ in the x-y-plane was calculated as $\varphi_{plane} = \arctan \frac{\alpha}{\beta}$. For the shift of the centers of the AOIs obtained with and without plane, the corresponding angle was calculated. In Fig. 3.10, the distribution of the differences of both angles $\Delta\varphi$ is plotted for the 280 laser images. Obviously, both angles are strongly correlated, which verifies the above explanation. (It should be noted, that two values of $\Delta\varphi$ where excluded in Fig. 3.10 for resolution reasons. Those two values where at $180° \pm 5°$)
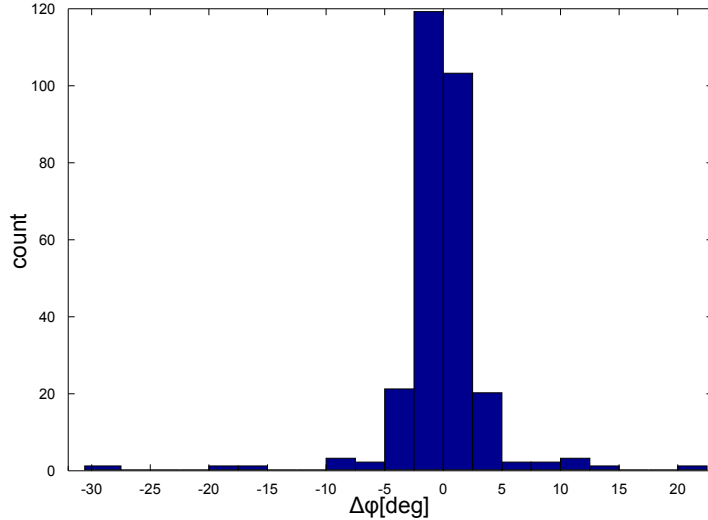
Figure 3.10: Histogram of the differences of the angles of plane gradient and shift of the AOI centers of the fits with and without plane. The narrow scattering of $\Delta\varphi$ around $0°$ implies a strong correlation. Two values around $180° \pm 5°$ where not included.

To sum up, fitting with a plane has to be dropped, although it produced better results for a handful of asymmetric laser spots as seen in Fig. 3.11. Due to the asymmetric underlying intensity distribution being described poorly by the Super-Gaussian alone, the actual edges and the edges of the AOI differ significantly in x. Fitting with a plane multiplied to the Super-Gaussian improved the matching remarkably for these laser spots. However, these improvements come at the cost of laser spots that were fitted well with only the Super-Gaussian. Since asymmetric spots significantly differ from the ideal case they should be avoided anyway. Also, the relative impact of a slightly biased AOI will be much smaller for them than for more flat-top like laser spots. Hence, it should be refrained from using the plane generally. It is possible to define a threshold that decides, whether to fit with or without plane. A good candidate would be the gradient of the plane, multiplied by the spot's diameter and divided by the height A, which roughly represents the intensity change by the plane, relative to the Super-Gaussian. However, due to the small number of affected laser spots and the small expected impact, this was not done here.

Despite some shortcomings, the fitting method has proven to be more predictable than the gradient method. Taking the underlying distribution into account makes it reliable and laser spots with different diffraction patterns and other inhomogeneities produce almost the same AOI, allowing comparable characterizations over a wide range of spots. Also information on the width of the flanks is obtained, which already is an important characterization parameter.

3.3 Filtering

Experiences from the fitting have shown, that for some laser spots, the AOI cannot be defined reasonably. This primarily applies to laser spots that do not have a flat-top profile but rather resemble a typical Gaussian. In most cases, this is either caused by a very small BSA size with subsequently large parts of the intensity being
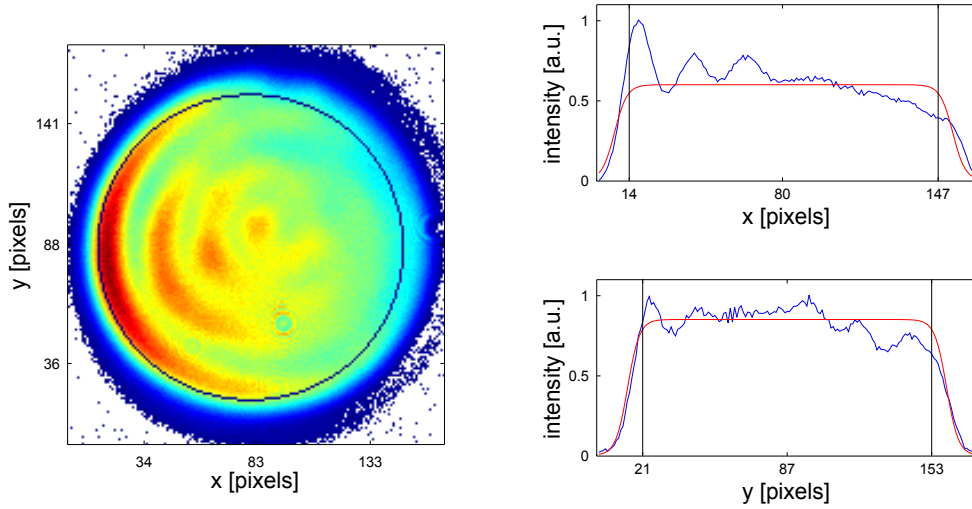
Figure 3.11: Laser spot with inhomogeneously illuminated BSA and AOI obtained by fitting without plane. In x, the edges of the AOI and the actual distribution do not match.
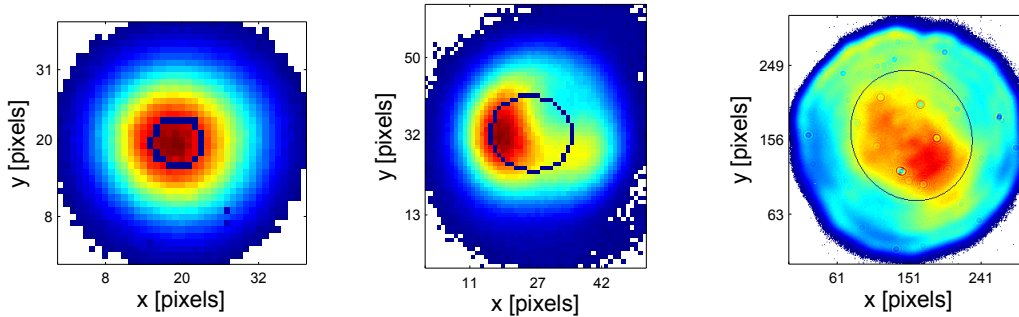

Figure 3.12: Non-flat-top laser spots with the AOI marked by blue ellipse. From left to right: Gaussian shape due to small BSA size, transition from Gaussian to flat-top shape with larger BSA, Gaussian shape due to large, inhomogeneously illuminated BSA. The AOI will not characterize the spots adequately.

cut by apertures or by very large BSAs which cannot be illuminated homogeneously and have a larger intensity in the center. Examples can be seen in Fig. 3.12. Usually the exponent G of the Super-Gaussian will then be rather small ($\lesssim 5$) and the flanks broad. In these cases, the AOI as defined above will only be a small area compared to the full laser spot (for small BSA size, it can be down to ≈ 20 pixels). In other cases, the AOI will be a small elliptical area with a large ratio of the semi-axes. In these cases, a further analysis of the AOI makes no sense since it can only have a minor effect on the emittance, not only because of its small share of the overall intensity, but also due to the spot's general deviation from the flat-top characteristic.

When required, these Gaussian like spots will have to be characterized with a different algorithm. It is, however, very likely that the degrading of the emittance due to the Gaussian shape will dominate over other manipulations, especially for small spots, where no additional diffraction pattern will appear. In that case, the exponent G obtained from fitting (see equation 3.7) might already be enough to characterize the laser spot. On the other hand, the spots inbetween Gaussian and flat-top shape were way to irregular to allow a universal characterization algorithm. Asymmetric spots like in Fig. 3.11 pose no major problem to the fitting algorithm.
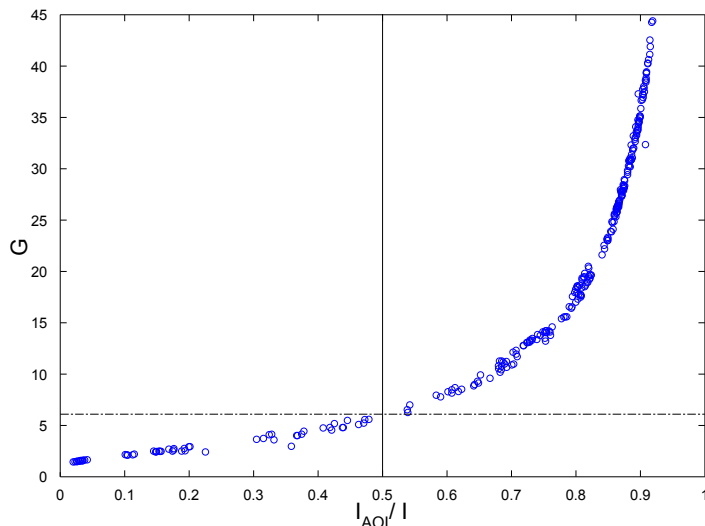
Figure 3.13: Super-Gaussian exponent (G) vs. intensity within AOI (I_{AOI}) over overall laser intensity I for all 280 laser images analyzed. The ratio $I_{AOI}/I = 0.5$ has proven to be the best threshold for filtering (not shown in this graph). The corresponding exponent G is an inferior threshold due to the small slope of G at this point.

Although it was discussed above, that the AOI can be shifted, the influence of this is rather small compared to the overall deviations from the flat-top shape.

Hence, it is reasonable to find characteristic parameters that allow the program to decide whether a further analysis should be conducted or not (or, if further studies suggest that the analysis of the Gaussian shaped spots is necessary, to decide which algorithm should be used). The following candidates for these characteristic were studied:

- χ^2 of the fit

- Super-Gaussian exponent G

- overall intensity $I = \sum_{ij} a(i,j)$

- overall intensity within the AOI

- standard deviation within the AOI

- fit function height A

- pixel count within the AOI

as well as various combinations of these parameters. The goal was to find a threshold in these parameters or their combinations as a decision basis. The classification of the spots by the threshold was compared to their fit result. Thereby no thresholds where accepted that produced false negatives (i.e. decided to not analyze although the fit result was reasonable), while false positives were tolerated though avoided.

The only parameters allowing a reasonable threshold were G and the ratio of the intensity within the AOI and the overall intensity $\frac{I_{AOI}}{I}$. Of course, both thresholds are correlated as shown in Fig. 3.13. The threshold of $\frac{I_{AOI}}{I} = 0.5$ has to be favored over $G = 6$, due to the small slope of G at that position. Even small variations in

G could lead to a different classification. Additionally, $\frac{I_{AOI}}{I}$ might give important meta information for the analysis, since it indicates the significance of the AOI.

Other attempts of filtering the spots failed. Matching the AOI size with the size of the actual BSA had to be given up, because the BSA sizes could not be reproduced reasonably anymore. Trials forcing a round fit and comparing it with the elliptical fit results bore no fruits either.

Fitting as well as filtering where developed on the basis of the 280 laser images taken between 23 March 2011 and 1 February 2012. Both were also tested with a set of 187 images taken between 2 March 2012 and 3 July 2012. The successful test with images not involved in the development speaks for the reliability of the algorithms. It should be noted that not all of these laser spots were actually used for operation, but a number of spots were used for alignment or were parts of error reports. Only a rough preselection has been conducted to avoid laser images with shapes far from real operation conditions.

Chapter 4

Laser beam characterization

Up to now the laser spots are characterized only by the BSA size and their rms size. Those obviously are not enough for a detailed analysis of the intensity distribution. There are a few obvious parameters that accomplish this:

Using the mean of the pixel values within the AOI

$$\bar{a} = \frac{1}{T} \sum_{i=1}^{N} \sum_{j=1}^{M} a(i,j) = \frac{1}{T} \sum_{ij} a_{ij} \tag{4.1}$$

with $T = N \cdot M$, the standard deviation of the pixel values is

$$\sigma_{a_{ij}} = \sqrt{\frac{1}{T} \sum_{ij} (a_{ij} - \bar{a})^2} \tag{4.2}$$

The standard deviation gives a measure of the variation of the pixel values around the mean. Since the goal is to characterize the influence of the inhomogeneities on the emittance, the relative variation needs to be considered, which is best described by $\sigma_{a_{ij}}/\bar{a}$. This corresponds to the standard deviation of a distribution normalized to have the mean $\bar{a} = 1$. This way the relative variations are comparable for different laser intensities. Though, the studies in [7, 8, 9, 10] have already shown, that this is not enough to characterize the beam with respect to the emittance growth.

Furthermore, it might be interesting to investigate the statistical distribution of the variations. Higher order moments of the distribution, like the skew [20]

$$\gamma = \frac{1}{T} \sum_{ij} \left(\frac{a_{ij} - \bar{a}}{\sigma_{a_{ij}}} \right)^3 \tag{4.3}$$

and the kurtosis [20]

$$k = \frac{1}{T} \sum_{ij} \left(\frac{a_{ij} - \bar{a}}{\sigma_{a_{ij}}} \right)^4 - 3 \tag{4.4}$$

are good tools to do this. The skew gives a parameter to discribe the asymmetry of a distribution. Any symmetric distribution has a skew of $\gamma = 0$ while a tail towards higher values amounts to a positive skew. A negative skew implies a tail towards lower values. The kurtosis measures the broadness of the distribution with the Gaussian distribution as a reference point $k = 0$. A positive kurtosis describes a distribution higher but narrower than the Gaussian distribution, but with wider

wings at its outer regions. Analogously, flatter, wider distributions have $k < 0$. Of course, these parameters only give information on the quantitative distribution of the variations and therefore are not sufficient, since they cannot distinguish between noise - which has no significant effect on the emittance - and large-area structures which decrease the electron beam quality.

Of course, not only the inhomogeneities of the flat-top part need to be analyzed. Also the general form is important. Here, the exponent G of the AOI fit function is important, especially for small BSA sizes, where G is relatively small and the distributions resembles more a Gaussian than a flat-top. This parameter might even provide the most important characterization for laser spots of this kind, that did not pass the filtering procedure. But even for the other laser spots, G (or its equivalent I_{AOI}/I as discussed in 3.3) will give an index of the significance of the flat-top analysis. Also the ratio of the semi-axes of the fit function should be considered. Note that the parameters σ_x and σ_y are not necessarily the semi-axes but need to be rotated according to σ_{xy}.

Further characterization parameters will be discussed in detail in the next sections.

4.1 Spatial Correlation

Parameters like rms error, kurtosis and skew describe the deviations between ideal and actual distribution. However, they are not able to describe the spatial distribution of these deviations. Specifically, it is not possible to distinguish between inhomogeneities in the intensity distribution and statistical noise using only these values. To quantify this distribution, a spatial correlation is suggested [9].

A covariance is defined by

$$\text{cov}(a, h) = \frac{1}{T} \sum_{ij} (a_{ij} - \overline{a}) \cdot (a_{ijh} - \overline{a}) \tag{4.5}$$

with a_{ijh} being the local mean of pixel values in the square of side length $2h + 1$ around a_{ij} (see Fig. 4.1)

$$a_{ijh} = \frac{1}{(2h+1)^2 - 1} \cdot \left(\sum_{l=-h}^{h} \sum_{k=-h}^{h} a_{i+lj+k} - a_{ij} \right) \tag{4.6}$$

$$=: \frac{1}{(2h+1)^2 - 1} \cdot \left(\sum_{lk} a_{i+lj+k} - a_{ij} \right) \tag{4.7}$$

In this definition the subtraction of a_{ij} avoids a direct dependence of a_{ijh} from a_{ij}. Finally the spatial correlation is defined by

$$\Lambda(a, h) = \frac{\text{cov}(a, h)}{\sigma_{a_{ij}}^2} \tag{4.8}$$

This can be regarded as the classical correlation coefficient between a_{ij} and a_{ijh} since it only differs in the normalization: for the correlation coefficient, $\sigma_{a_{ij}}^2$ in Eq. 4.8 needs to be replaced by $\sigma_{a_{ij}} \cdot \sigma_{a_{ijh}}$. This definition was chosen because it proved to be more sensitive for high brightness beams with a good homogeneity and gave a greater range of variation [21]. It will be shown, that it also makes a distinction

27

Figure 4.1: Illustration for the definition of a_{ijh}. Pixel values within the gray area are averaged to obtain a_{ijh}.

between noise and large scale inhomogeneities. Due to this feature, this definition will be studied in detail.

To understand the difference from the standard definition of the correlation coefficient, first assume two data sets a and a' with the same correlation coefficient:

$$\frac{\sigma_{ah}}{\sigma_{a_{ij}}\sigma_{a_{ijh}}} = \frac{\sigma'_{ah}}{\sigma'_{a_{ij}}\sigma'_{a_{ijh}}} \tag{4.9}$$

where σ_{ah} is the covariance between a_{ij} and a_{ijh}. Since a better differentiation of both sets is desired, assume without loss of generality that the corresponding alternative definitions are different in the way

$$\frac{\sigma_{ah}}{\sigma_{a_{ij}}^2} < \frac{\sigma'_{ah}}{\sigma'^2_{a_{ij}}} \tag{4.10}$$

This leads to

$$\frac{\sigma_{ah}}{\sigma_{a_{ij}}^2} = \frac{\sigma_{ah}}{\sigma_{a_{ij}}\sigma_{a_{ijh}}} \cdot \frac{\sigma_{a_{ijh}}}{\sigma_{a_{ij}}} = \frac{\sigma'_{ah}}{\sigma'_{a_{ij}}\sigma'_{a_{ijh}}} \cdot \frac{\sigma_{a_{ijh}}}{\sigma_{a_{ij}}} < \frac{\sigma'_{ah}}{\sigma'^2_{a_{ij}}} \tag{4.11}$$

$$\Rightarrow \frac{\sigma_{a_{ijh}}}{\sigma'_{a_{ijh}}\sigma_{a_{ij}}} < \frac{1}{\sigma'_{a_{ij}}} \tag{4.12}$$

$$\Rightarrow \frac{\sigma'_{a_{ij}}}{\sigma'_{a_{ijh}}} < \frac{\sigma_{a_{ij}}}{\sigma_{a_{ijh}}} \tag{4.13}$$

Equation (4.13) shows that the definition of the spatial correlation as in [9] will be lower for data sets with a higher ratio of $\sigma_{a_{ij}}/\sigma_{a_{ijh}}$. This obviously is a good approach, since $\sigma_{a_{ijh}}$ describes the standard deviation of large areas, i.e. it primarily

contains the underlying intensity distribution, whereas $\sigma_{a_{ij}}$ is the standard deviation of single pixels and also includes noise and statistical variations. Therefore a higher ratio between both implies a higher ratio between noise and actual inhomogeneities. This again implies the noise having a higher relative influence on the covariance. Favoring this over the influence of inhomogeneities is of course sensible for a spatial correlation.

While it is obvious, that for noise dominated intensity distributions $\sigma_{a_{ij}}$ will be larger than $\sigma_{a_{ijh}}$, it has to be proven that this is generally the case. To do so, the definitions of both have to be compared:

$$\sigma_{a_{ij}} = \sqrt{\sum_{ij} \frac{a_{ij}^2}{T} - \bar{a}_{ij}^2} \qquad\qquad \sigma_{a_{ijh}} = \sqrt{\sum_{ij} \frac{a_{ijh}^2}{T} - \bar{a}_{ijh}^2} \qquad (4.14)$$

First, the mean of the local average is

$$\bar{a}_{ijh} = \sum_{ij} \frac{a_{ijh}}{T} = \sum_{ij} \frac{\left(\sum_{lk} a_{i+lj+k} - a_{ij}\right)}{T[(2h+1)^2 - 1]} \qquad (4.15)$$

On the right side of equation (4.15) the inner sum adds up all pixel values in a square of side length $2h+1$ around a_{ij}. The outer sum repeats this for every i and j, subtracting a_{ij}. This way, neglecting the borders of the data set, every pixel value will be added up as often as there are pixels in the square around a_{ij}. Knowing this, equation (4.15) can be rewritten as

$$\bar{a}_{ijh} = \sum_{ij} \frac{(2h+1)^2 a_{ij} - a_{ij}}{T[(2h+1)^2 - 1]} = \sum_{ij} \frac{a_{ij}}{T} = \bar{a}_{ij} \qquad (4.16)$$

So the average of all pixel values and the average of the local mean are the same. The difference of the standard deviations in equation (4.14) reduces to the sums. These have to be analyzed in detail.

Looking at the definition of the statistical variance $V(x)$

$$V(x) = \frac{1}{N_x} \sum_{i} (x_i - \bar{x})^2 \qquad (4.17)$$

it is obvious that $V(x) \geq 0$. Since equation (4.17) can be rewritten as $V(x) = \overline{x^2} - \bar{x}^2$ this results in

$$\bar{x}^2 \leq \overline{x^2} \qquad (4.18)$$

or, to put it in words, the mean of the squares is always larger than the square of the mean.

For easier handling, the sum in $\sigma_{a_{ijh}}$ in equation (4.14) can be transformed to

$$\sum_{ij} \frac{a_{ijh}^2}{T} = \sum_{ij} \frac{\left(\sum_{lk} a_{i+lj+k} - a_{ij}\right)^2}{T[(2h+1)^2 - 1]^2} = \sum_{ij} \frac{\left(\sum_{lk \neq 0} a_{i+lj+k}\right)^2}{T[(2h+1)^2 - 1]^2} \qquad (4.19)$$

Applying equation (4.18) to the right side of equation (4.19)

$$\sum_{ij} \frac{a_{ijh}^2}{T} = \sum_{ij} \frac{\left(\sum_{lk \neq 0} a_{i+lj+k}\right)^2}{T[(2h+1)^2 - 1]^2} \leq \sum_{ij} \frac{\sum_{lk \neq 0} a_{i+lj+k}^2}{T[(2h+1)^2 - 1]} \qquad (4.20)$$

Again using the fact that inner and outer sum add up every a_{ij}^2 exactly $(2h+1)^2-1$ times, this can be rewritten to

$$\sum_{ij} \frac{a_{ijh}^2}{T} \leq \sum_{ij} \frac{[(2h+1)^2-1]a_{ij}^2}{T[(2h+1)^2-1]} = \sum_{ij} \frac{a_{ij}^2}{T} \qquad (4.21)$$

$$\Rightarrow \sum_{ij} \frac{a_{ijh}^2}{T} \leq \sum_{ij} \frac{a_{ij}^2}{T} \qquad (4.22)$$

$$\Rightarrow \sigma_{a_{ijh}} \leq \sigma_{a_{ij}} \qquad (4.23)$$

This way, the spatial correlation $\Lambda(a,h)$ will always be between -1 and 1 since its absolute value will always be smaller than the absolute value of the correlation coefficient.

It should be noted that in practice $\Lambda(a,h)$ will not have relevant negative values. A negative $\Lambda(a,h)$ implies that for the majority of pixels, a pixel value a_{ij} above average $\bar{a}$ has a corresponding local average a_{ijh} below $\bar{a}$ and vice versa. This is possible for noise dominated distributions with $a_{ijh} \approx \bar{a}$. However, in this case $\Lambda(a,h)$ will be approximately zero. An attempt to construct a theoretical distribution with $\Lambda(a,h)$ well below zero failed.

In [9], pixel values outside the - differently defined - AOI, that need to be included in a_{ijh}, are assumed to be equal to the mean of the whole AOI, to avoid boundary problems. This is legitimate, since the intensity distributions of the SPARC laser are relatively uniform, in particular it is completely lacking the diffraction patterns observed at PITZ. The inhomogeneities seem to come from the illumination of the BSA only. However, this will not work for the PITZ laser. The diffraction pattern usually has its highest values at the edges , where the boundary problems will appear. Calculating the local average by assuming some pixels to be equal to the global mean of the AOI will strongly bias the results towards lower values for Λ. For this reason, pixels outside the AOI are simply not included in the calculation of a_{ijh}. This way, only the statistical representativity of a_{ijh} is reduced by the smaller size of the sample, but a systematic bias is avoided.

It needs to be discussed, whether to actually use the mean $\bar{a}$ for the calculation, or to replace it with the result of the Super-Gaussian fit $f_{SG}(i,j)$. This might be useful since the fit result is meant to describe the underlying intensity distribution, which might be a better point of reference. However, one needs to bear in mind, that it still does not describe the ideal case.

Calculations show that σ usually is larger when calculated with the fit result as can be seen in Fig. 4.2. This is probably due to the fact that at the edges, the fit result has smaller values, but at the same positions, the outer ring of the diffraction pattern has its highest values. The differences of both get even more pronounced by the squaring. Since the standard deviation σ_{mean} is smaller in most cases, the mean describes the flat-top part of the laser images better. These effects carry over to the spatial correlation (Fig. 4.3). Here again, the values calculated with the fit result tend to be larger. The reasons are probably the same as for σ, although the covariance is already divided by σ^2 to obtain the spatial correlation Λ. Therefore $\text{cov}(a,h)$ seems to be even more affected.

All in all, it was decided to use the mean for the calculations instead of the fit result. The differences have been too large to be neglected (up to 10% of the resulting
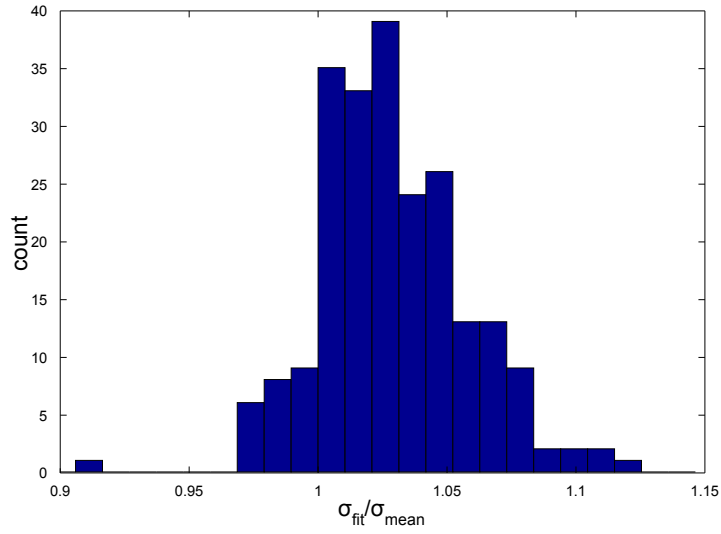
Figure 4.2: Histogram of the ratios of the rms error calculated with the fit result σ_{fit} and the standard deviation σ_{mean}. The histogram shows that $\sigma_{fit} > \sigma_{mean}$ in most cases.
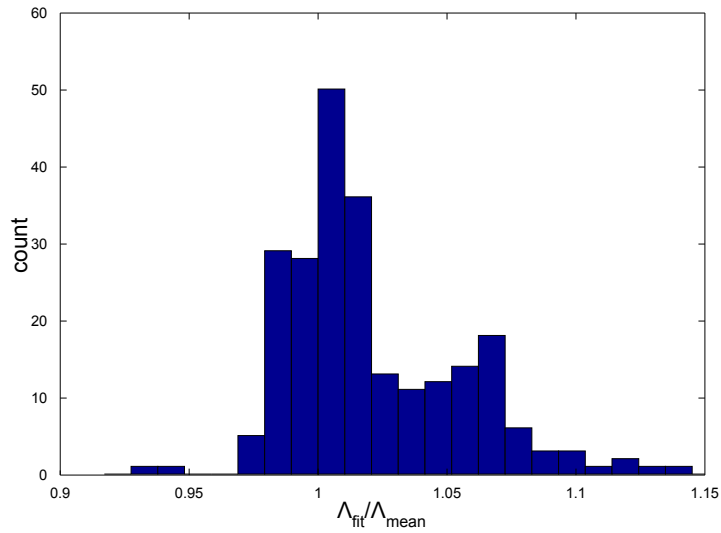

Figure 4.3: Histogram of the ratios of the spatial correlations calculated with the fit result and with the mean. As for the rms, values calculated with the fit result tend to be larger.

values) and all statistical features of the rms and the spatial correlation (as discussed in the appendix) can only be reasoned with the mean $\bar{a}$ applied. Also one has to bear in mind, that the fit result describes a realistic underlying intensity distribution but not the ideal case, so its meaning in the analysis of the inhomogeneities is rather unimportant.

Finally an appropriate value for h needs to be found. $2 \cdot h$ is the size of the square in which the local average a_{ijh} is calculated. Therefore it acts as a resolution for the spatial correlation. Structures significantly smaller than this square will be averaged out or at least their influence will be toned down. Ideally, h needs to be smaller than the smallest structure to be resolved. Basically this is the working principle of the spatial correlation since noise has the smallest 'structures' of down to 1 pixel. On the other hand, h must not be chosen too small. For laser spots with low statistical noise, the pixels immediately around a_{ij} will have about the same value as a_{ij}, so the smaller h is chosen, the more a_{ijh} will converge towards a_{ij} and the spatial correlation will converge towards $\Lambda = 1$. In this case, the variations in Λ will be too small and too dominated by noise in order to make a reasonable distinction between different laser spots.

In order to have a consistent significance of the spatial correlation for different spot sizes, the resolution - and thereby h - needs to be chosen relative to the spot size. Otherwise, for different spot sizes, structures with different relative size (i.e. influence on the emittance) will be weighted equally. Then the interpretation of the spatial correlation would depend on the spot size, which is undesirable. In [9], a ratio of $N/h = 20$ was found to be optimal for the SPARC laser system. A wide variation in Λ for a better distinction (achievable with small N/h) and a minimum resolution (large N/h) have been the decisive criteria. Here, N can roughly be considered the diameter of the laser spot. Since the spots of the PITZ laser system are assumed to be possibly elliptical, N is redefined as $N = \sigma_x + \sigma_y$ with σ_x and σ_y from the AOI fit function. For the spots analyzed in this work, this is a good approximation for the N used in [9], since all of the spots were approximately circular. However, if the ratio of the 'semi-axes' σ_x and σ_y is significantly different from 1 or σ_{xy} is large, this will not work properly anymore. In this case a possible solution might be different values for h in x and y, of course with respect to the rotation of the actual semi-axes induced by σ_{xy}. In Fig. 4.4, histograms of the spatial correlation are presented for different ratios of N/h. Obviously, for the PITZ laser, $N/h = 20$ does not give a satisfying variation. The widest variation is seen for $N/h \approx 10$. This is due to the different laser spots measured at PITZ and SPARC. While the PITZ laser produces the strong diffraction pattern discussed above, no such pattern can be seen in the SPARC images, where the inhomogeneities seem to stem from the illumination of the BSA only. Due to the good uniformity of the SPARC laser, a larger N/h had to be chosen in [9] to resolve smaller features of the intensity distribution. The diffraction pattern, which often makes up the major factor for the inhomogeneities of the PITZ laser, usually has relatively large structures, so the resolution does not have to be as fine.

In Fig. 4.5, two laser spots are shown with almost the same BSA size. In the lower left diagram, Λ is plotted against N/h. Here, a major disadvantage of the spatial correlation shows up. Despite the fact, that the right spot is notably more uniform, the spatial correlation is always higher (i.e. worse). That is because Λ - as defined in equation 4.8 - is calculated relative to the standard deviation σ, which is much smaller for the right spot. Without further analysis, no decision on
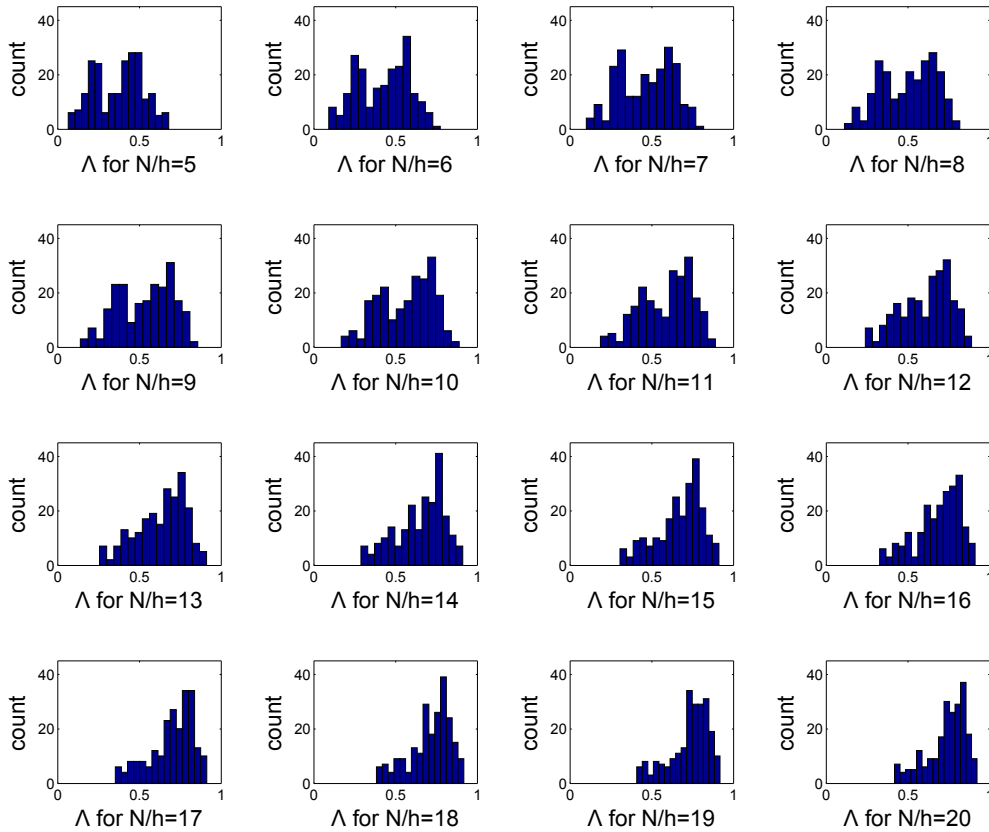
Figure 4.4: Histograms of Λ calculated for different values of N/h. Unlike the result of [9] the widest variation is around $N/h = 10$, while for $N/h = 20$ the spatial correlations concentrate at higher values. The reason for this are the differences in the analyzed laser spots. The SPARC laser images are more uniform than the PITZ laser images and show no noticable diffraction pattern.

which parameter is more important for the emittance can be made. Also it is very likely, that there is an overlap, i.e. for spots with similar standard deviation, the spatial correlation might be the critical parameter, while in general a lower standard deviation is better. Therefore it is suggested, to use the relative covariance

$$\varrho = \frac{\text{cov}(a, h)}{\overline{a}^2} \tag{4.24}$$

as a characterization parameter, with $\text{cov}(a, h)$ as defined in equation 4.8. For the two spots in Fig. 4.5, ϱ is plotted in the lower right diagram, against N/h. Here the better homogeneity of the right laser spot becomes apparent at the first glance, which makes it the superior parameter e.g. for operation staff of the accelerator, in case it proves to be relevant for the emittance. It combines most the information of the spatial correlation (spatial distribution of the inhomogeneities) and the standard deviation (general height of these inhomogeneities) and therefore might even replace both parameters in the characterization.

Ultimately, no decision for a value of N/h can be made without simulations investigating the effect of the different values of Λ and ϱ on the emittance and the dependency on N/h. On the other hand, calculating Λ for different values of N/h might be even more interesting. By doing so, laser spots are analyzed with different resolutions, which can give additional information on the spatial distribution of the inhomogeneities, e.g. if the inhomogeneities are small-scale structures or large-scale
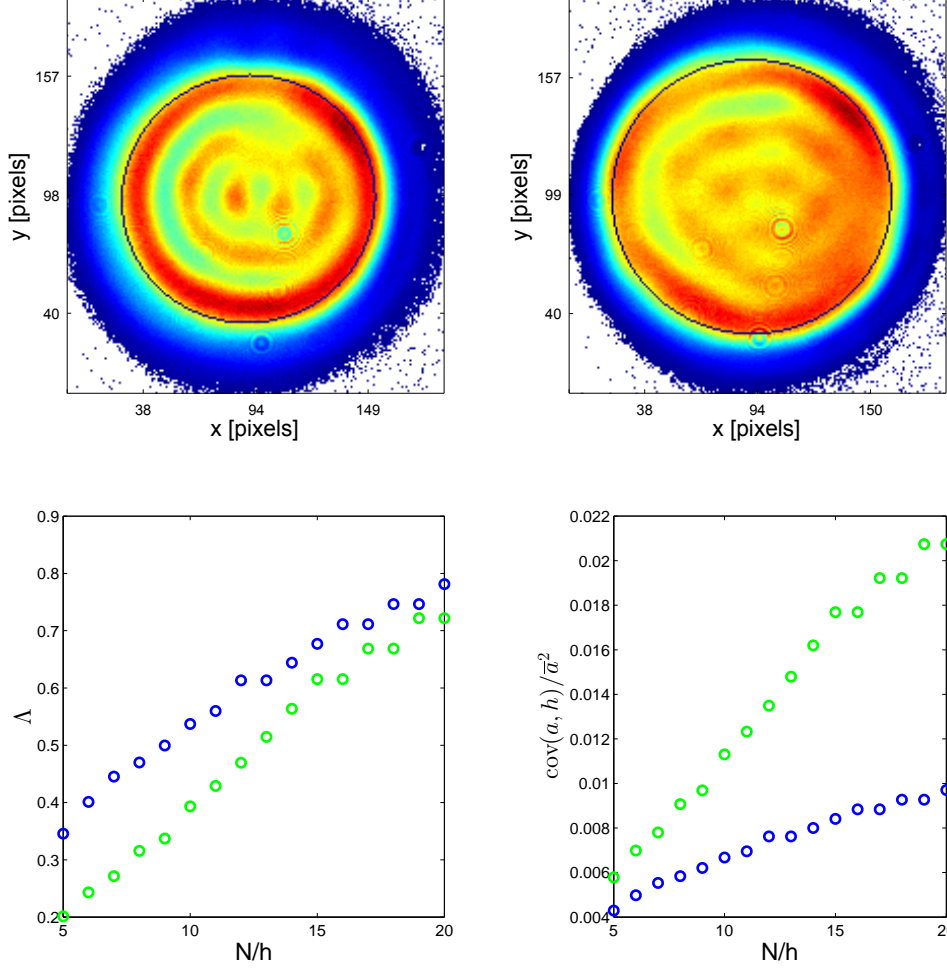
Figure 4.5: Two laser spots with similar BSA size but different standard deviation: $\sigma_{left}/\overline{a} = 0.17$ and $\sigma_{right}/\overline{a} = 0.11$. Below are the spatial correlation Λ and the relative covariance $\mathrm{cov}(a,h)/\overline{a}^2$ plotted against N/h (green: left spot, blue: right spot). While the spatial correlation alone indicates, that the right spot is worse, the relative covariance shows that it actually is more uniform than the left spot. The reason for this difference is the relativity of Λ to the standard deviation. (Note that the steps occur when a change in N/h causes no change in the rounded h.)

asymmetries. The steeper slope and lower values in Λ in Fig. 4.5 indicate, that the inhomogeneous structures of the left spot have a smaller scale than the structures of the right spot.

4.2 Expansion in Fourier and Bessel series

With the spatial correlation and the relative covariance, parameters have been introduced, that, one the one hand, can quantify the spatial distribution of inhomogeneities and on the other hand also can provide information on their size. Nevertheless both parameters are still purely statistical quantities. Now its is interesting to investigate the actual intensity distribution directly. In particular, integral transforms are of interest, that transform the laser spots into spectra. The most obvious candidate is of course the Fourier transform, especially since the diffraction pattern can be explained by Fourier optics. However it will not be possible to calculate
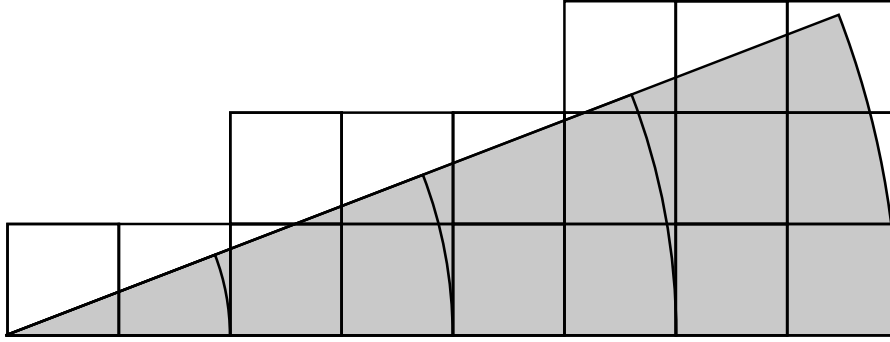
Figure 4.6: Information loss during transform from cartesian to polar coordinates due to discrete data. For large r, several pixels (i, j) will contribute to a single coordinate (r, φ), for small r, a single pixel (i, j) will be included in various (r, φ)-duplets.

some kind of "effective BSA" (i.e. an aperture in the Fourier plane equivalent to the actual limiting apertures) from the laser spots, since half of the information relevant to Fourier optics - the phase - is lost during the measurement, that only can measure the absolute intensity values. For this reason, other transforms might prove to be interesting as well. Here, a transform on the base of Bessel functions of the first kind is recommendable, due to the circular nature of most laser spots.

At this point it should be discussed, which parts of the spot need to be transformed. Of course the transform will only involve the AOI, since the structures on the flat top are of particular interest. Thus the analysis must be done in polar coordinates, with due regard to the elliptic distortion. The problem is, that for an analysis in polar coordinates, the data has to be transformed from cartesian to polar coordinates. Since the original data is discrete, information loss is inevitable as can be deduced from Fig. 4.6. The most simple methode, calculating (i, j) for a given (r, φ) and using the pixel value next to this coordinate - e.g by rounding (i, j) - has to be dropped, because in this way, statistical fluctuations and noise will play a major role. On the other hand, defining an area for every (r, φ) and averaging over this area will require much effort and when it comes to small values of r, the area will still be too small to have a sufficient statistical basis. To avoid this, the original data was smoothed. Every pixel was assigned the mean of pixel values in a square around it, similar to a_{ijh} in the previous section, only without eliminating a_{ij}. The side length of the averaging square was chosen to be $1/30$ of the diameter of the AOI, which usually ranges between 4 and 10 pixels. Here again, structures smaller than this square will not be resolved but such structures will have no significant impact on the emittance either.

To take the elliptical shape of the AOI into account, first, the actual semi-axes need to be calculated. The rotated ellipse as defined in eq. 3.6 can be represented by the matrix [20]

$$M = \begin{pmatrix} \sigma_x^2 & \sigma_{xy} \\ \sigma_{xy} & \sigma_y^2 \end{pmatrix} \tag{4.25}$$

which can be rotated by an angle θ

$$M' = R^T \cdot M \cdot R \tag{4.26}$$

with R the rotation matrix

$$R = \begin{pmatrix} \cos\theta & -\sin\theta \\ \sin\theta & \cos\theta \end{pmatrix} \tag{4.27}$$

An ellipse with the semi-axes along x- and y-axis has the form

$$M' = \begin{pmatrix} r_x^2 & 0 \\ 0 & r_y^2 \end{pmatrix} \tag{4.28}$$

With the matrix elements $M'(1,2) = M'(2,1) = 0$, the rotation angle can be calculated as

$$\theta = \frac{1}{2}\arctan\frac{2\sigma_{xy}}{\sigma_x^2 - \sigma_y^2} \tag{4.29}$$

With this, the semi-axes r_x and r_y can be calculated. In polar coordinates, the ellipse is described by the distance from the center

$$d(\varphi) = \frac{r_x r_y}{\sqrt{r_x{}^2 \sin\varphi + r_y{}^2 \cos\varphi}} \tag{4.30}$$

Using this, elliptical coordinates can be transformed into cartesian coordinates. In polar coordinates, r refers to a circle with the fixed radius r. In order to remain consistent, in the elliptical coordinates (r, φ), r will not refer to the distance d from the center but to the ellipse with the smaller semi-axis r.

The main goal of this work is to characterize the inhomogeneities of the laser spot, i.e. the variations from the ideal flat-top. Therefore, the mean $\bar{a}$ (see equation 4.1) was subtracted from the data before transform, so only the variations from that mean will be analyzed.

The Fourier transform for finite, discrete data $f(t)$ is defined as

$$c_n = \frac{1}{T}\sum_{t=0}^{T-1} f(t) \cdot e^{-2\pi i \frac{nt}{T}} \tag{4.31}$$

In order to use Bessel functions of the first kind $J_\nu(r)$ as a base for integral transforms, it has to fulfill two requirements: They need to be orthogonal and the vector space spanned by the Bessel functions needs to include the function to be transformed, i.e. the set of Bessel functions needs to be complete. The orthogonality is given for the scalar product

$$\int_0^b J_\nu\left(\alpha_{\nu m}\frac{r}{b}\right) J_\nu\left(\alpha_{\nu n}\frac{r}{b}\right) r \mathrm{d}r = \delta_{nm}\frac{b^2}{2}\left[J_{\nu+1}(\alpha_{\nu m})\right] \tag{4.32}$$

where $\alpha_{\nu m}$ is the mth zero of $J_\nu(r)$. The completeness of $J_\nu\left(\alpha_{\nu n}\frac{r}{b}\right)$ is proven by Watson ([22], p. 591f) in the interval $(0, b)$. With this, any function $f(r)$ can be expanded in the series

$$f(r) = \sum_{m=1}^{\infty} c_{\nu m} J_\nu\left(\alpha_{\nu m}\frac{r}{b}\right) \tag{4.33}$$

with $r \in (0, b)$, $\nu \geq 0$ and the coefficients $c_{\nu m}$

$$c_{\nu m} = \frac{2}{b^2[J_{\nu+1}(\alpha_{\nu m})]^2}\int_0^b f(r)J_\nu\left(\alpha_{\nu m}\frac{r}{b}\right) r \mathrm{d}r \tag{4.34}$$

being the transform of $f(r)$ [23].

While this transform is named Fourier-Bessel series expansion (or Hankel transform for $b \to \infty$), it will hereafter be referred to as Bessel transform, whereas the term Fourier-Bessel transform will refer to a successive Fourier transform in one dimension of a two-dimensional field and a Bessel transform in the other dimension, as it will be discussed below.

The next step will be the coordinate transformation in two dimensions. The Fourier transform in two dimensions can be written as

$$F(k,l) = \frac{1}{\sqrt{MN}} \sum_{m=0}^{M-1} \sum_{n=0}^{N-1} f(m,n) e^{-2\pi i \left(\frac{mk}{M} + \frac{nl}{N} \right)} \tag{4.35}$$

$$= \frac{1}{\sqrt{M}} \sum_{m=0}^{M-1} f'(m,l) e^{-2\pi i \frac{mk}{M}} \tag{4.36}$$

with

$$f'(m,l) = \frac{1}{\sqrt{N}} \sum_{n=0}^{N-1} f(m,n) e^{-2\pi i \frac{nl}{N}} \tag{4.37}$$

being the 1D Fourier transform of $f(m,n)$ in n for all M columns. This shows, that a two-dimensional Fourier transform can be accomplished by simply applying two successive 1D Fourier transforms, one in each dimension. Fourier-Bessel transforms can be derived analogously, taking into account, that the Bessel transform works in real space only.

Concerning the two-dimensional transform, the obvious choice for the transform in φ is the Fourier transform, because the data is periodic in φ. If a Bessel transform is applied in φ, the result will strongly depend on the definition of $\varphi = 0$ and will change with any change in the mapping from cartesian to polar coordinates. Therefore, only the option of Fourier-Bessel transform and Fourier-Fourier transform need to be discussed.

The Bessel transform was implemented in the code as derived in eq. 4.34, with the integral replaced by a sum to adapt for the discrete data. The zeros $\alpha_{\nu m}$ are calculated with the third party MATLAB function ZEROBESS [24], which uses the Newton-Raphson method. Although MATLAB has a build in Fourier transform function fft, a custom Fourier transform was written according to eq. 4.31, to allow for better control of the code. Both functions where then separately tested for functionality and accuracy. To accomplish this, the Fourier and Bessel weights c_n and $c_{\nu m}$ where generated randomly within $[-0.5, 0.5]$. Then, a sample was calculated by adding up Bessel or cosine functions according to the weights. Afterwards, the sample was analyzed with the written transform functions. For the Fourier transform, the differences between initial weights and result were within one order of magnitude to the floating-point relative accuracy (MATLAB command eps), hence the Fourier transform is considered to be accurate and working. However, it should be noted, that for arbitrary functions used as samples, the Fourier transform was not as accurate. The error from the analytic result increased with n, due to the discretization. Still the difference from the built-in Fourier transform was marginally. For the Bessel transform, things look different. In Fig. 4.7 the random weights and the result of the transform are plotted, as well as the difference between both. The difference shows a characteristic curve that looks like an exponential slope. So unlike the Fourier transform, the Bessel transform comes with an error even for data
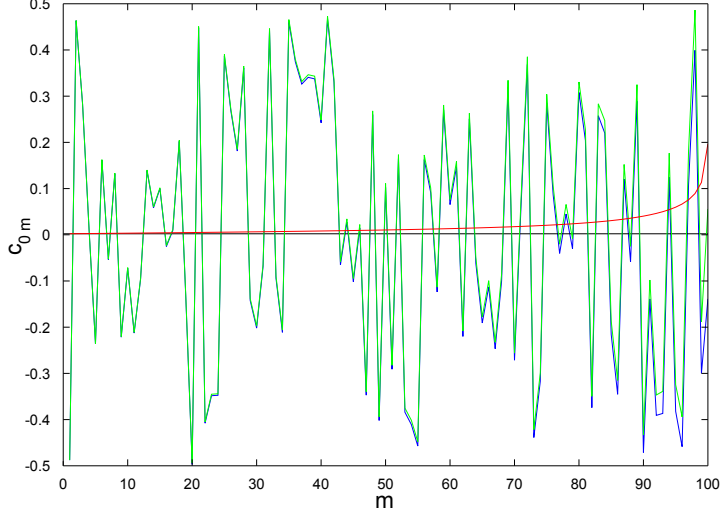
Figure 4.7: Randomly generated Bessel weights (blue) and the result of the Bessel transform of the sample (green). The difference (red) shows the characteristic behavior, though slope and extent differ widely.

calculated from its base functions. This will be examined in more detail. Since the difference curve varied significantly, the process of randomly generating the Bessel weights, calculating the sample and transforming it was repeated 1000 times. For the 1000 curves, the absolute mean was calculated and is shown in Fig. 4.8. However, the slope depends on the length of the sample (i.e. m_{max}). For smaller m_{max}, the curve is steeper and the errors larger. The characteristic curve implies that the Bessel transform is relatively accurate for smaller m (smaller "frequencies") and gets worse for higher frequencies, i.e. shorter periods. Since equation 4.34 is exact, this is obviously caused by replacing the integral with a sum to allow for discrete data.

$$c_{\nu m} = \frac{2}{b^2 [J_{\nu+1}(\alpha_{\nu m})]^2} \sum_{r=0}^{b} f(r) J_\nu \left(\alpha_{\nu m} \frac{r}{b} \right) r \qquad (4.38)$$

For the sizes m and n faced in this work, the Fourier transform is considered much more accurate than the Bessel transform, so for the two-dimensional Fourier-Bessel transform, the Fourier transform will be conducted first.

It is important to remember some fundamental differences between the Fourier and Bessel transform, when interpreting the following diagrams. First off, when interpreting the Bessel functions $J_{\nu m}$ as somewhat periodic functions, m and the index of the Fourier coefficients, n, are not the same. For Bessel functions, m is the number of zeros within the range of data, while for $e^{-2\pi i \frac{nt}{T}}$, n is the number of periods, which always have 2 zeros. This means, the Bessel functions have a smaller "resolution" of only one zero (or one maximum), while for the Fourier transform, the resolution is doubled (for an odd number of zeros k, the Fourier transform will produce a broader spectrum around $n = k/2$). This has the effect, that for a data set of length l, the maximum number of Bessel coefficients $m_{max} = l$, while for the Fourier coefficients, $n_{max} = l/2$. This is because a maximum (or a zero) needs at least one pixel to be reproduced, one period (2 zeros) needs at least 2 pixels. Any higher frequency will produce a kind of stroboscopic effect that will be analyzed as a lower frequency. Anyhow, it is unlikely that these restrictions will pose a problem, since structures smaller than several pixels are probably noise and will be lost during
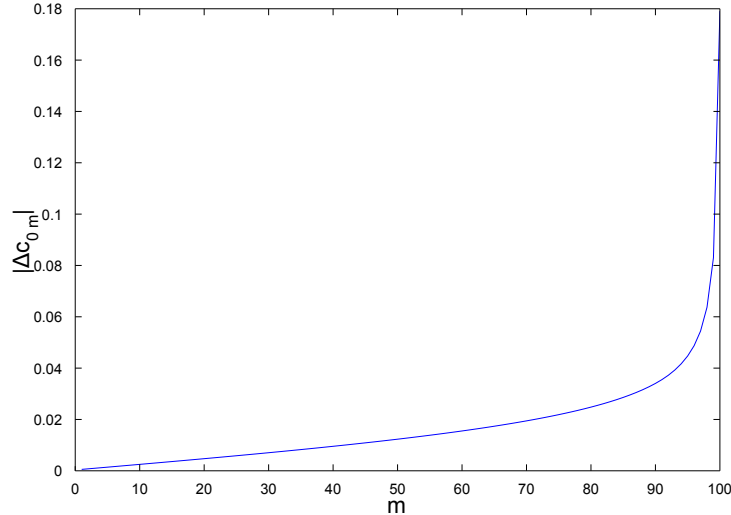
Figure 4.8: Absolute difference between randomly generated Bessel weights and result of the Bessel transform averaged over 1000 samples with $m_{max} = 100$. The Bessel weights were within $[-0.5, 0.5]$

the smoothing and subsequent transform to elliptical coordinates.

Another important difference is the fact, that the Fourier transform is able to account for an offset, which is simply represented by c_0. The Bessel transform on the other hand does not have an offset coefficient, because a constant function is not orthogonal to the Bessel functions. Any offset from a superposition of Bessel functions will add the Bessel transform of a constant to the spectrum, which is rather broad. Unfortunately, the actual spectrum and the offset spectrum cannot be separated. However, there is a possibility to cope with this problem. As mentioned earlier, the set of Bessel functions is only complete in $(0, b)$. This is because at the point $r = b$, $J_\nu \left(\alpha_{\nu m} \frac{r}{b} \right) = J_\nu(\alpha_{\nu m}) = 0$. Also, $J_\nu(0) = 0$ for every $\nu > 0$. Only $J_0(0) \neq 0$. Since it is unlikely, that the sample has the same value at $r = 0$ and $r = b$, in the following, only J_0 was examined further. For this reason, the index ν will not be written anymore, every reference to the Bessel transform implies $\nu = 0$. Now, the sample can be provided with an artificial offset that enforces the element at $r = b$ to be 0. With this trick, the Bessel functions J_0 have a chance to describe the modified sample completely. Therefore it is assumed, that the artificial offset is the best estimation for the value, around which the Bessel functions are fluctuating. In fact, later comparisons showed a cleaner, narrower spectrum. However, it needs to be kept in mind, that the sample was biased in an arbitrary way to comply with the base functions of the transform.

In Fig. 4.9 - 4.11 three exemplary laser spots are presented together with their 1D Fourier transforms in the azimuthal angle φ and their 2D Fourier-Bessel transforms. For the Fourier transforms in φ, the absolute values are shown, because $c_n(r)$ is complex for $n \neq 0$. Only $c_0(r)$ (the average of every column of r in (b)) always has real values and is therefore presented with its sign. The 2D Fourier-Bessel transforms were calculated from these real $|c_n(r)|$ values and are presented in (e) and (f). While using the absolute values of $c_n(r)$ is not exactly a 2D Fourier-Bessel transform, it makes interpretation easier: The result represents the Bessel transform of the weights of the respective Fourier base functions without regarding the phase. If desired, the phase can be extracted and transformed separately.
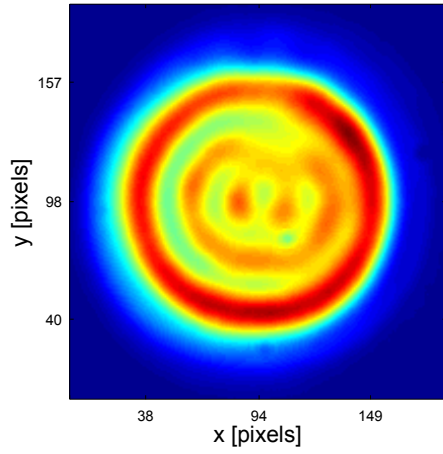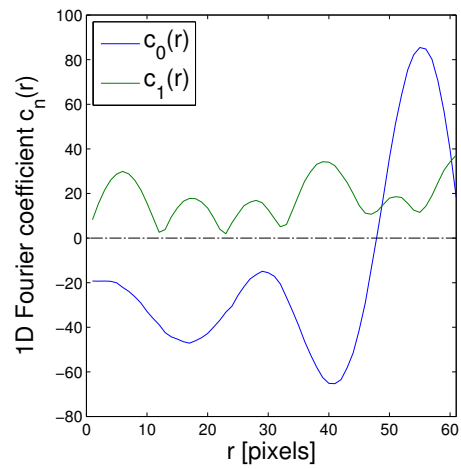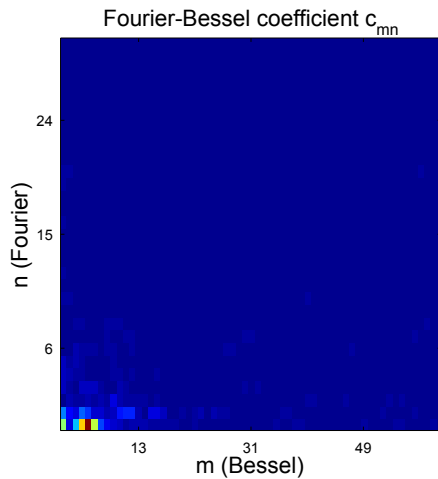
(a) Smoothed Laser spot
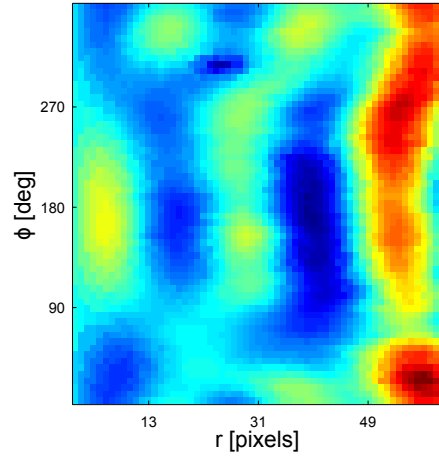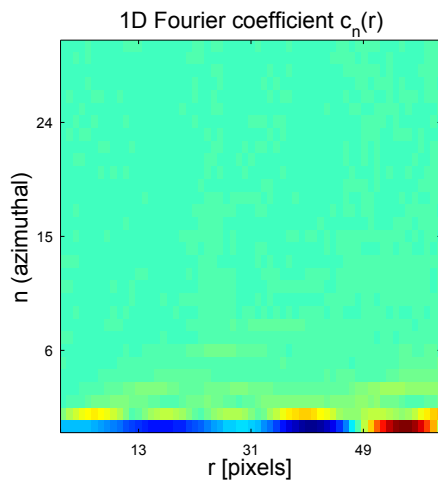
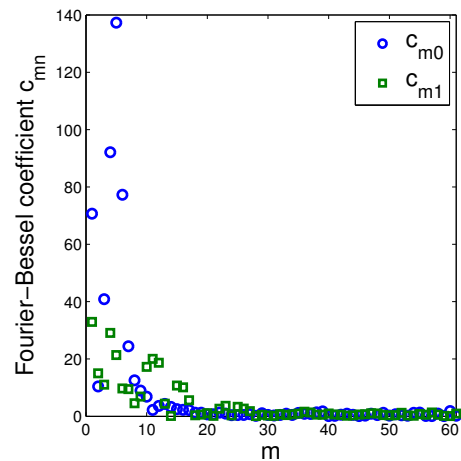(b) AOI in polar coodinates with $\bar{a}$ subtracted.

(c) Fourier tranform in φ

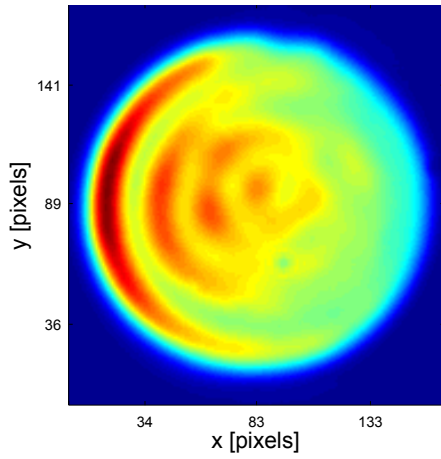(d) $c_0(r)$ (blue) and $c_1(r)$ (green) of the Fourier transform in φ. (see (c))

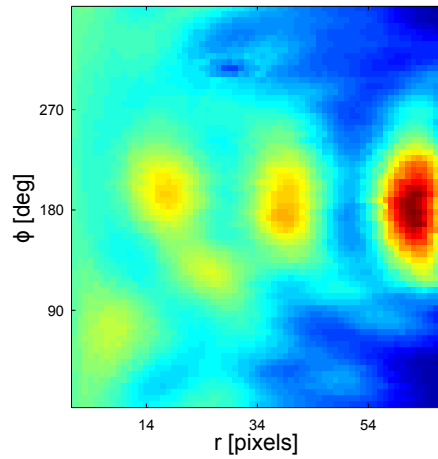(e) Fourier-Bessel transform

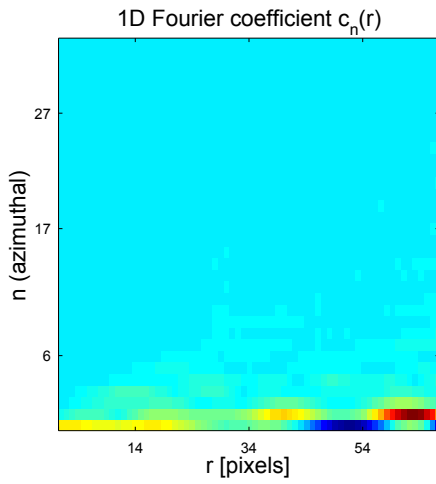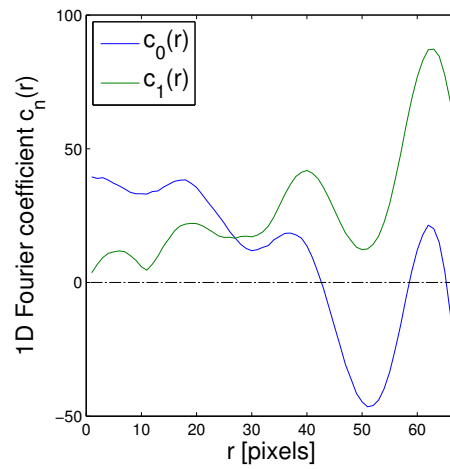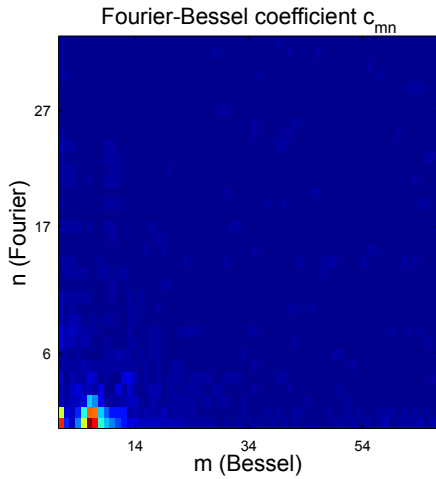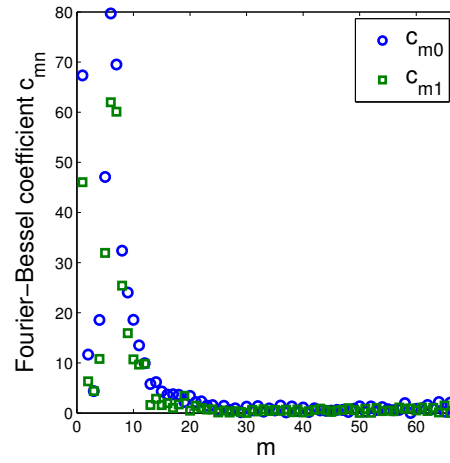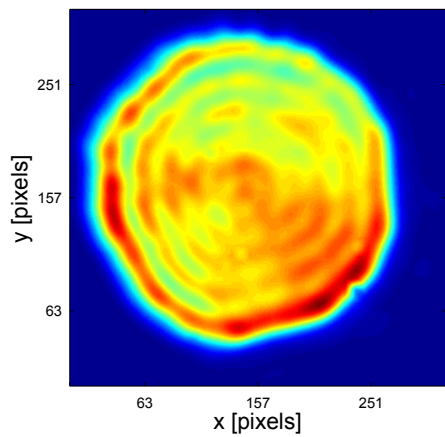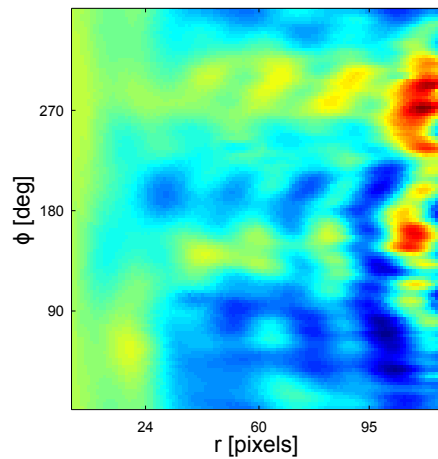(f) c_{m0} (blue) and c_{m1} (green) of the Fourier-Bessel transform.

Figure 4.9: Laser spot in cartesian (a) and polar (b) coordinates. The Fourier transform in φ (c)(d) is the first step of the Fourier-Bessel transform. The Fourier-Bessel coefficients in (e) are the result of the Bessel transform of the Fourier coefficients $c_n(r)$ in (c) along r. Equally, (f) represents the Bessel transform of (d) in r.

(a) Smoothed Laser spot

(b) AOI in polar coodinates with $\bar{a}$ subtracted.

(c) Fourier tranform in φ

(d) $c_0(r)$ (blue) and $c_1(r)$ (green) of the Fourier transform in φ. (see (c))

(e) Fourier-Bessel transform

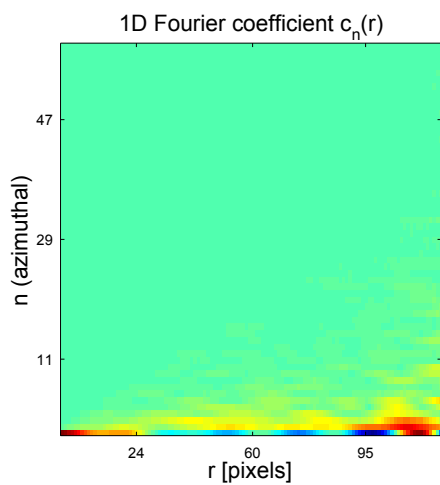(f) c_{m0} (blue) and c_{m1} (green) of the Fourier-Bessel transform.

Figure 4.10: Laser spot in cartesian (a) and polar (b) coordinates. The Fourier transform in φ (c)(d) is the first step of the Fourier-Bessel transform. The Fourier-Bessel coefficients in (e) are the result of the Bessel transform of the Fourier coefficients $c_n(r)$ in (c) along r. Equally, (f) represents the Bessel transform of (d) in r.
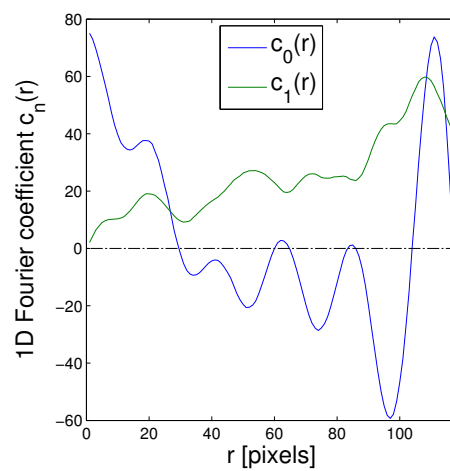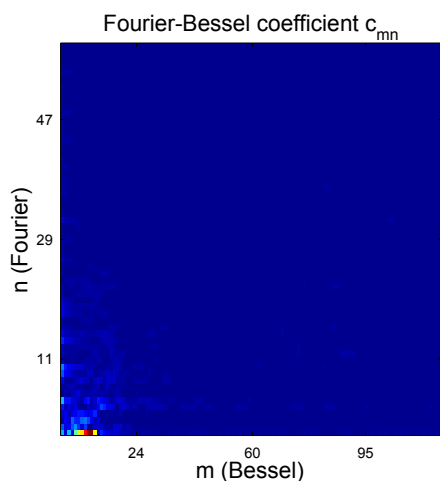
(a) Smoothed Laser spot
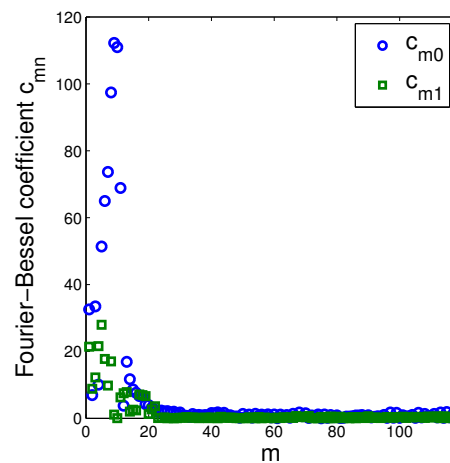
(b) AOI in polar coodinates with $\bar{a}$ subtracted.

1D Fourier coefficient $c_n(r)$

(c) Fourier tranform in φ

(d) $c_0(r)$ (blue) and $c_1(r)$ (green) of the Fourier transform in φ. (see (c))

Fourier-Bessel coefficient c_{mn}

(e) Fourier-Bessel transform

(f) c_{m0} (blue) and c_{m1} (green) of the Fourier-Bessel transform.

Figure 4.11: Laser spot in cartesian (a) and polar (b) coordinates. The Fourier transform in φ (c)(d) is the first step of the Fourier-Bessel transform. The Fourier-Bessel coefficients in (e) are the result of the Bessel transform of the Fourier coefficients $c_n(r)$ in (c) along r. Equally, (f) represents the Bessel transform of (d) in r.

Unfortunately, the spectra obtained by Fourier-Bessel transform are anything but narrow line spectra. Adjusting the values at $r = b$ (as discussed above) has narrowed the spectra significantly, so lines can be identified along m. However, those lines are rather broad. An influence of the limited accuracy of the Bessel transform discussed above can be denied, since the errors are small for small values of m, the important part of the spectra. The separated but broad lines imply, that the data can roughly be described by Bessel functions corresponding to the centers of these lines. Nevertheless, these Bessel functions need to be modified in their form to comply with the data, hence the broadness. This means, Bessel functions are not the best choice for the transform along r, since those are practically just counting the maxima. In principle, a 2D-Fourier transform should be able to do at least the same, while relying on the more intuitive sine and cosine functions.

For the same laser spots, the two-dimensional Fourier transforms are presented in Fig. 4.12. Here again, the second transform was performed with the absolute values of the result of the first transform, except for $n = 0$. As with the Fourier-Bessel transform, the spectra are broad and unhelpful. In fact, the spectra look even broader than the ones of the Fourier-Bessel transform, though this is only due to the smaller resolution of the Fourier transform mentioned above.

Neither the Fourier-Bessel transform, nor the 2D-Fourier transform offer much useful information to be extracted from the spectra. On the other hand, it makes no sense to use the whole transform of a laser spot for its characterization. It has to be kept in mind, that the aim of this work is, to provide information that helps operation staff in optimizing the laser spot, resulting in the best achievable emittance of the electron beam. In order to do this, systematic measurements or simulations have to be conducted to correlate parameter values or features of diagrams to the emittance growth. This will become harder, if not impossible, the more complex the information gets and the harder it is to interpret. For the broad spectra of two dimensional transforms, it is unlikely that universally valid relations can be found. Therefore, the Fourier-Bessel transform und 2D-Fourier transform have to be dropped as means of laser characterization.

With this, the two most promising two-dimensional integral transforms have disqualified. However, the approach should not be set aside completely. A focus should be set on the one-dimensional Fourier transform in φ as seen in Fig. 4.9(c) - 4.11(c). The meaning of $c_n(r)$ can be understood easily. When plotted against n, it is simply the Fourier transform of one column of the laser spot displayed in polar coordinates, i.e. the spectrum of sine and cosine waves constituting that column. If plotted against r, as in Fig. 4.9(d) - 4.11(d), it displays the weight of a certain angular frequency n over the course of r.

The presented 1D Fourier transforms show that the main part of the inhomogeneities is made up of frequencies with $n \lessapprox 10$. Coefficients with larger n only manipulate the shape of the lower frequency inhomogeneities or are statistical variations. For further analysis, the Fourier transform can therefore be reduced to $n \leq 10$. Unfortunately, still several hundred values remain, which is far to much for a useful characterization. Information has to be reduced somehow, while keeping important characteristics of the laser spot. An interesting candidate is a projection of the absolute values of $c_n(r)$ on n: $\sum_r |c_n(r)|$. This will represent the complete influence of the frequency n on the laser spot. Comparing this for different n should give characteristic information on distribution of inhomogeneities on the spot. However, it needs to be kept in mind, that for a small r, the relative influence is much
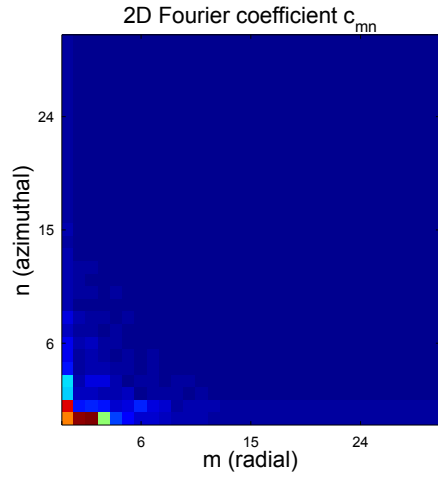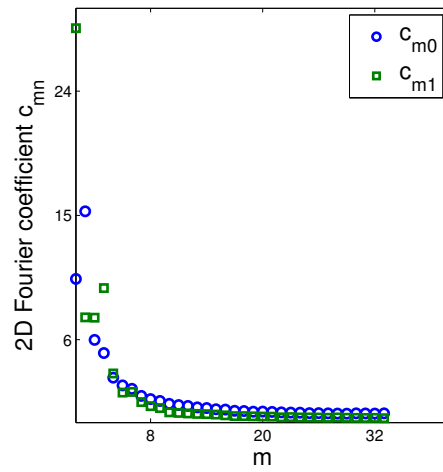
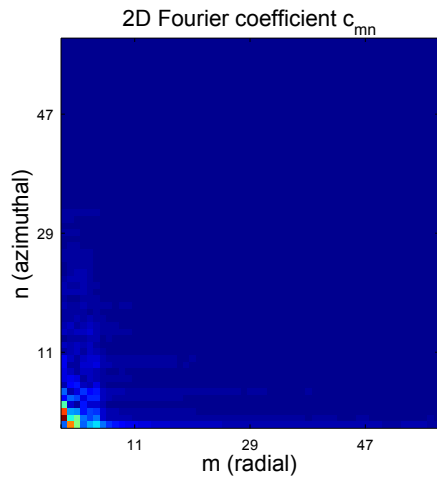(a) Two-dimensional Fourier transform of the laser spot in Fig. 4.9
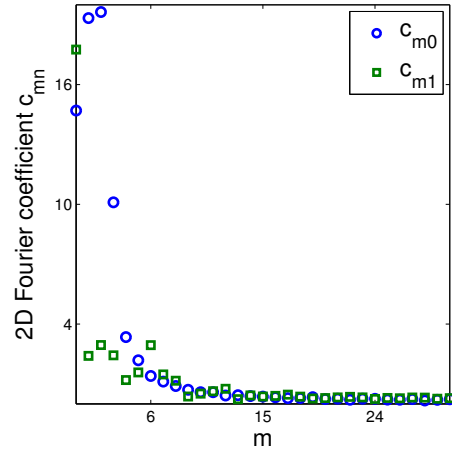
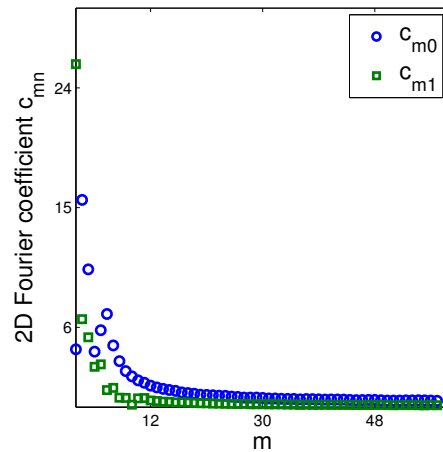(b) c_{m0} (blue) and c_{m1} of the 2D Fourier transform.
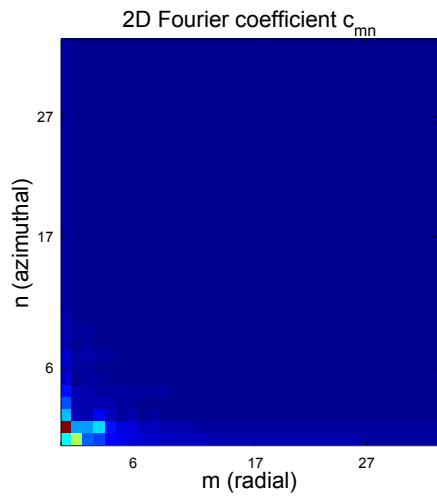
(c) Two-dimensional Fourier transform of the laser spot in Fig. 4.10

(d) c_{m0} (blue) and c_{m1} of the 2D Fourier transform.

(e) Two-dimensional Fourier transform of the laser spot in Fig. 4.11

(f) c_{m0} (blue) and c_{m1} of the 2D Fourier transform.

Figure 4.12: Two-dimensional Fourier transforms of the laser spots shown in Fig. 4.9 - Fig. 4.11. The left side represents the 1D Fourier transform in r of the 1D Fourier transform in φ (Fig. 4.9(c) - Fig. 4.11(c)). On the right side, the Fourier transforms of Fig. 4.9(d) - Fig. 4.11(d) are presented.

smaller than for a large r. Hence, the coefficients $c_n(r)$ need to be weighted by the relative area they cover, e.g. $\pi \cdot \left[r^2 - (r - \Delta r)^2\right] / A_{AOI}$ (with A_{AOI} the area of the AOI) for circular spots. Also, the projection needs to be divided by the average of the AOI, in order to compare the relative magnitude of $c_n(r)$ for various laser spots. So, for a round laser spot, the projection is calculated as

$$p(n) = \sum_r \frac{|c_n(r)| \cdot \pi \left[r^2 - (r - \Delta r)^2\right]}{A_{AOI} \cdot \overline{a}} \qquad (4.39)$$

with the average of the AOI $\overline{a}$. Nevertheless, this projection cannot suffice as a characterization of the spatial intensity distribution as it neglects an important part of the result of the Fourier transform: the phase contained in the complex values. It is possible to think of laser spots with the same projection $p(n)$ but completely different characteristics. This can easily be done for any laser spot by arbitrarily choosing a section along r (e.g. ring of arbitrary width for round spots) and rotating it around the center by an arbitrary angle. A simplified, hypothetical example for this is shown in Fig. 4.13(a) and 4.13(b). Both spots have only one azimuthal frequency of $n = 1$. While the phase for the left, relatively symmetric spot changes over r, it is independent of r for the right spot. Although the spots differ significantly, both have the same projection $p(n)$. To cope with this, the complex projection is introduced:

$$p_c(n) = \left| \sum_r \frac{c_n(r) \cdot \pi \left[r^2 - (r - \Delta r)^2\right]}{A_{AOI} \cdot \overline{a}} \right| \qquad (4.40)$$

It differs from $p(n)$ in that the coefficients $c_n(r)$ are added up as complex numbers. Interpreting complex numbers as vectors on the complex plane, this means, that the complex coefficients $c_n(r)$ are still added up like in $p(n)$ if all of them have the same phase (i.e. direction in the complex plane). If on the other hand, the phases differ, they will be added up like vectors, possibly canceling each other, so $0 < p_c(n) < p(n)$. In other words, a large value of $p_c(n)$ means, that the frequency n determines the global image of the laser spot and has a clear footprint in the profiles. A small value implies phase shifts along r and stronger small scale variations but better global symmetry. Therefore, by comparing $p(n)$ and $p_c(n)$ a method is provided to distinguish between small scale and large scale inhomogeneities in φ.

In Fig. 4.13, this can be seen: the left, more symmetric spot has a complex projection $p_c(n)$ significantly smaller than $p(n)$ because the phase of the azimuthal sine is changing over r. For the right, highly asymmetric spot, the phase is constant over r, thus $p_c(n) \approx p(n)$.
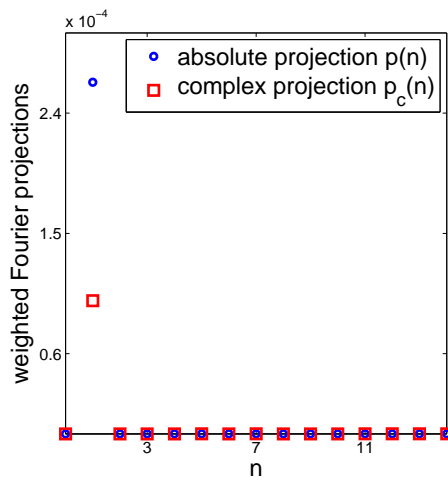
In Fig. 4.14 the weighted Fourier projections of the spots shown in Fig. 4.9 - 4.11 are presented. It is interesting to interpret the spectra: The spot 4.14(a) has a relatively broad spectrum with $p(n)$ decreasing with n, which means, the higher frequencies are primarily modifying the form of the lower frequency modulations. However, with $p_c(n)$ being significantly lower than $p(n)$ for the dominating frequency $n = 1$, this does not dominate the whole picture that much. The raised value in p(3) suggests 3 local maxima along φ in a limited range of r. The spot in Fig. 4.14(b) has a very narrow spectrum with the dominating frequency $n = 1$ almost unmodified. As expected, $p_c(1) \approx p(1)$, which is obviously due to the asymmetry of the laser spot. The third spot 4.14(c) again has a very broad, decreasing spectrum, but unlike spot 4.14(a), this spectrum dominates the overall picture, since $p_c(n) \approx p(n)$ for the dominating frequencies.
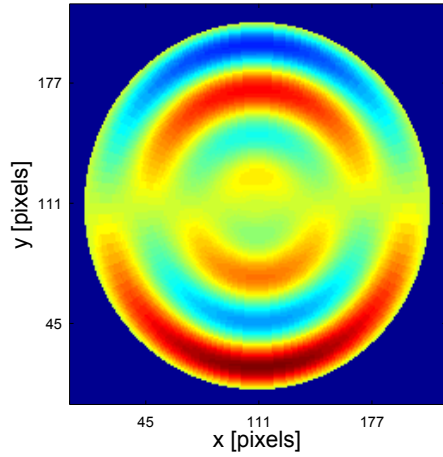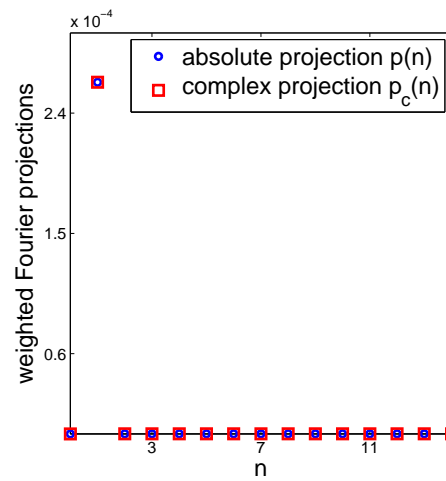
(a) Constructed, relatively symmetric laser spot with the only azimuthal frequency of $n = 1$.
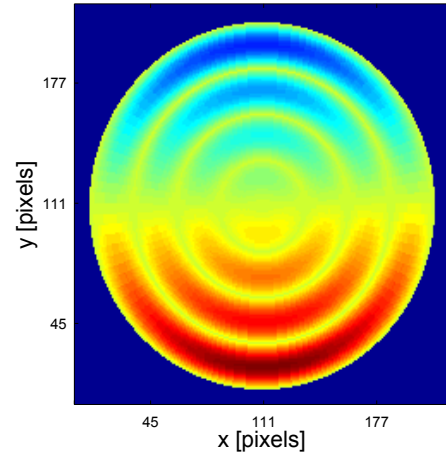
(b) Constructed asymmetric laser spot with the only azimuthal frequency of $n = 1$.

(c) Weighted Fourer projections $p(n)$ and $p_c(n)$. The projections differ significantly.

(d) Weighted Fourer projections $p(n)$ and $p_c(n)$. Both projections are the same.

Figure 4.13: Weighted Fourier projections for constructed symmetric and asymmetric laser spots. Both spots have an azimuthal frequency of $n = 1$ and a radial frequency of $m = 2$. However, both look very different due to different phases of the periods in φ. For the more symmetric spot, the phase was constant over r, while for the asymmetric spot, the phase switched between 0 and π with every half period along r.
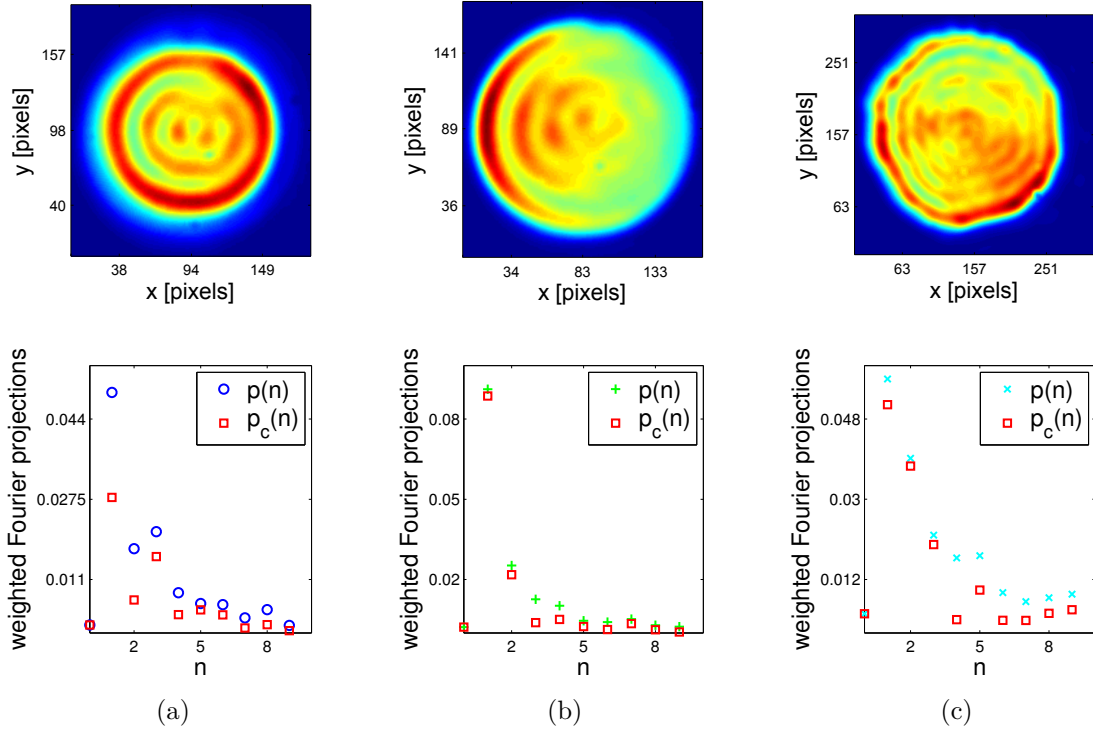
Figure 4.14: Weighted Fourier projections of the laser spots shown in Fig. 4.9 - 4.11.

Of course, the spectra also should be compared directly, as in Fig. 4.15. Since all of the spots are dominated by the azimuthal frequency $n = 1$ while the spot in Fig. 4.14(a) has the lowest $p(1)$ it must be considered the most homogeneous spot in terms of rotational symmetry.

As mentioned above, comparing $p(n)$ and $p_c(n)$ allows to distinguish between small scale and large scale inhomogeneities in φ. However, if $p_c(n)$ in fact is small compared to $p(n)$, i.e. the inhomogeneities are on a smaller, non-global scale, no conclusions on the actual scale can be made: while it is clear, that the phases change over the course of r, the frequency of this change is completely unknown yet. To get a grasp of the radial frequencies, the one dimensional Fourier transform along the radius, $c_m(\varphi)$ can be used. Here again, a projection is the best choice to compress the information. However, this time, no weighting is necessary, since every φ is similar. The radial projection is then calculated as

$$p_r(m) = \frac{\Delta\varphi}{2\pi\overline{a}} \sum_{\varphi} |c_m(\varphi)| \tag{4.41}$$

where $\frac{\Delta\varphi}{2\pi}$ is the inverse of the number of steps in φ, which makes $p_r(m)$ the average relative Fourier coefficient $p_r(m) = \frac{\overline{c_m}}{\overline{a}}$.

The radial projections for the laser spots discussed above are presented in Fig. 4.16. For the spot (a) the relatively large values of $p_r(m = 1..3)$ suggests a radial frequency of about $m = 2$. The spectrum for spot (b) looks similar, but the smaller value for $p_r(2)$ indicates more separate frequencies of $m = 1$ and $m = 3$. Spot (c) shows two isolated frequencies: a dominating one with $m \approx 1$ and a smaller one with $m \approx 5$. While it is possible, to compare the coefficients of one spot to distinguish between major, minor and modifying frequencies, the spectra of different laser spots should not be compared. The reason for this can be seen, when comparing the
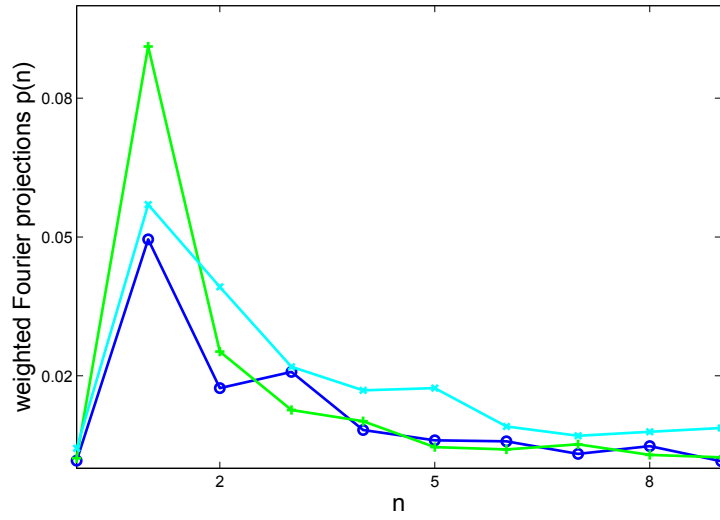
Figure 4.15: Comparison of the weighted Fourier projections $p(n)$ of the laser spots above. The spot in Fig. 4.14(a) (blue) has the lowest dominating frequency and can therefore be considered the most rotationally homogeneous spot, the more so because of its small $p_c(n)$.
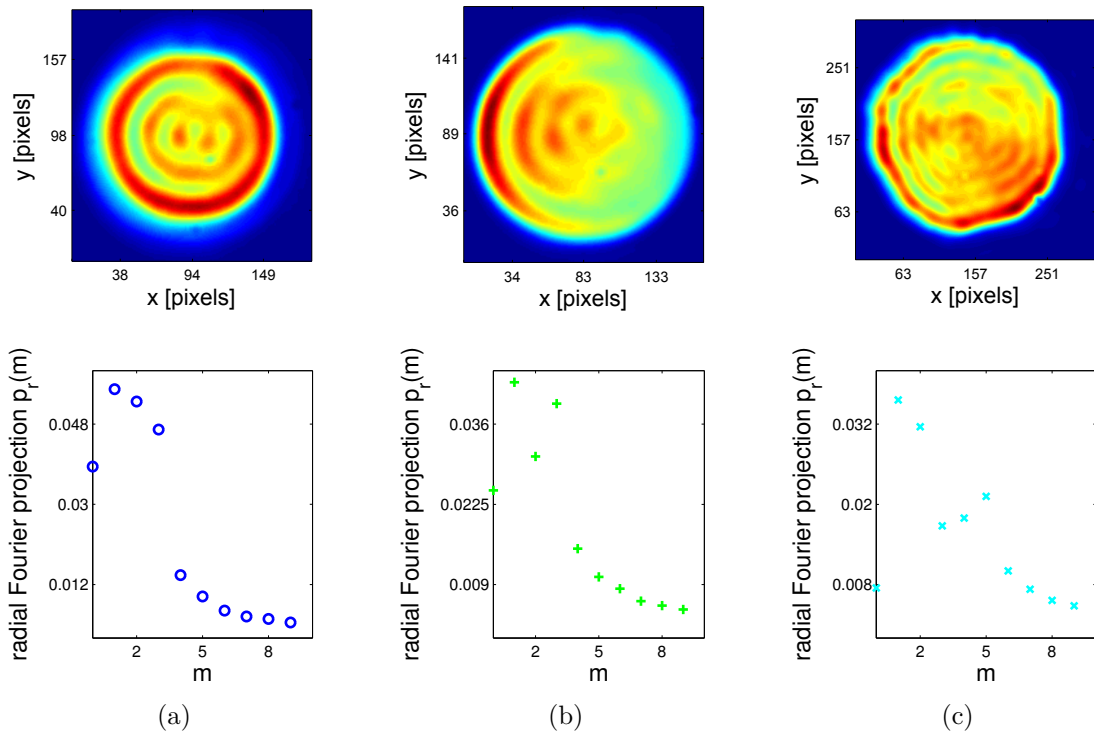

Figure 4.16: Radial Fourier projections of the laser spots shown in Fig. 4.9 - 4.11.

spectra of the spots (a) and (b): the values of $p_r(m)$ are much larger for spot (a) than for (b), which suggest, (b) is more homogeneous in r. However, the relative height of the inhomogeneities is roughly similar. The reason for this mismatch is the averaging in the calculation of $p_r(m)$: while the azimuthal asymmetry of (b) will also have an impact on the radial projection, it will diminish at the point of the azimuthal zero-crossing, thereby reducing the average. Another reason to be careful when interpreting $p_r(m)$ is that the spectrum does not describe the fluctuations around the actual average $\bar{a}$, but around the calculated value $\bar{a} + c_0(\varphi)$ for every φ. This is, because for the Fourier transform along r, every value along r is weighted equally, which leads to a wrong average in polar coordinates, hence $c_0(\varphi) \not\approx 0$ and $p_r(0) \not\approx 0$. A third reason for the limited value of $p_r(m)$ for characterization purpose is, that the spectrum highly depends on the definition of the AOI. If the AOI is chosen to be larger (e.g. everything larger that 80% of the fit function maximum), the fluctuations will have a smaller relative size, compared to the AOI and the the spectrum will shift to larger m.

Therefore, the radial projection $p_r(m)$ should only be considered as additional information to the weighted azimuthal Fourier projections discussed above. Its mere purpose is to provide an estimate of the radial frequencies to determine the scale of the inhomogeneities, if $p_c(n) << p(n)$. Unlike for $p(n)$, it is not useful, to calculate a complex projection for the radial Fourier transform, similar to $p_c(n)$, since a phase shift can occur when the center of the AOI is not exactly the center of the diffraction pattern. Also, a phase change would have no impact on the scale of the inhomogeneities along r.

The relatively broad spectrum of the radial Fourier projection in Fig. 4.16(a) raises the question, if the Bessel transform is the better choice to calculate $p_r(m)$. In that case, $c_m(\varphi)$ in equation 4.41 would not represent the Fourier transform but the Bessel transform along r. The advantage is the better resolution of the Bessel transform as discussed before. The radial Bessel projections $p_r(m_B)$ of the laser spots discussed above are shown in Fig. 4.17. Note that $2m_B \hat{=} m$. As expected, the lines of the spectra are better separated than in the radial Fourier projection. The broad Fourier spectrum of spot (a) stems from a single maximum $m_B = 1$ which would have an equivalent $m = 1/2$ in the Fourier projection. Since m can only have integer values, this is substituted by a combination of $m = 0..2$. This is broadened up further by the second line around $m_B = 5$. The other spots are described in a better detail as well. However, this comes at a price: the Bessel function J_0 has decreasing maxima. To describe data with invariable maxima, the lines have to broaden up and in fact, the signs of the coefficients are alternating. So the larger m_B gets, the broader the lines will get, and the higher they will become, although the corresponding fluctuations have a constant size. This means, the relative impact of the different lines can not be estimated from the radial Bessel projections, but only in the radial Fourier projections (Fig. 4.16). Hence, the radial Bessel projection $p_r(m_B)$ must be seen as complementary information to the radial Fourier projection $p_r(m)$.
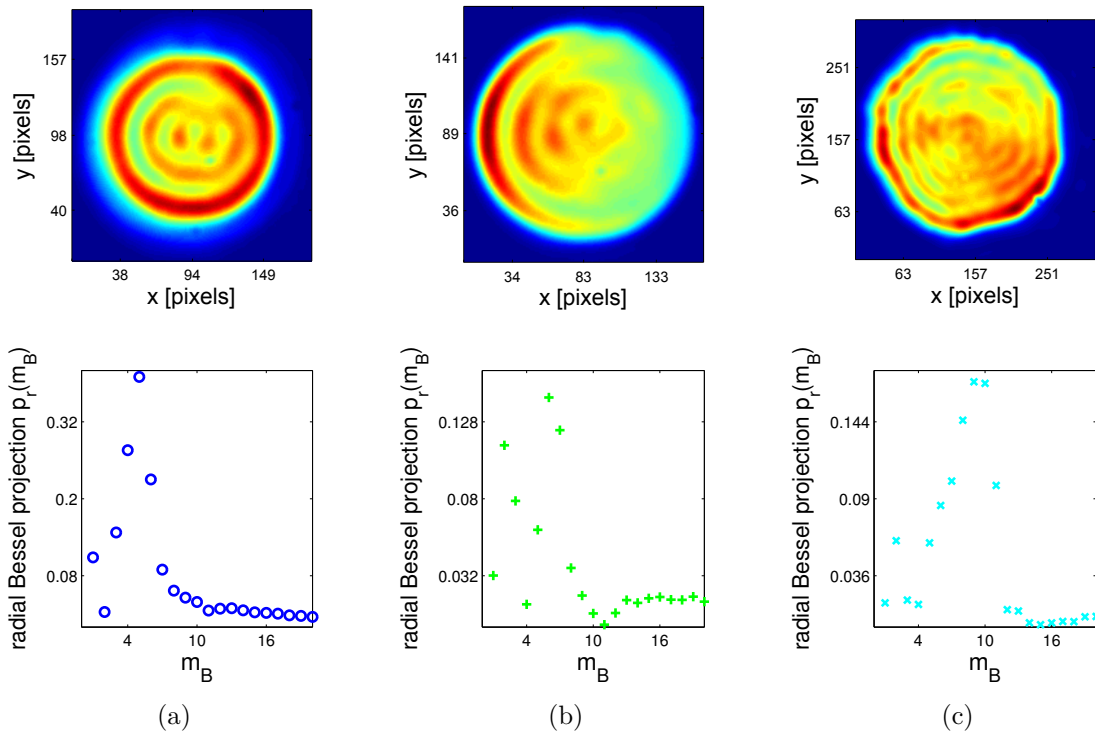
Figure 4.17: Radial Bessel projections of the laser spots shown in Fig. 4.9 - 4.11. A better separation of the lines can be observed, but the relative impact can not be compared anymore.

Chapter 5

Summary and Outlook

In this work, an algorithm has been developed, that locates the laser spots autonomously and reliably defines an area of interest. No human intervention is necessary and the result is reproducible. This algorithm has successfully been tested for an independent "control group".

For the characterization, various parameters have been suggested, that describe the general form of the laser spot (exponent G of the Super-Gaussian fit function and the ratio of the semi-axes) as well as the uniformity of the flat-top part. Here, the most important parameters are the relative standard deviation $\sigma_{a_{ij}}/\overline{a}$, that quantifies the height of the inhomogeneities, and the spatial correlation Λ or the relative covariance ϱ, that classify the spatial distribution and areal extend, thereby separating relevant inhomogeneities from noise and small scale structures.

With the weighted Fourier projection $p(n)$, a tool is provided, that measures azimuthal inhomogeneities according to the area they cover which is equivalent to their overall impact. Coupled with the complex Fourier projection $p_c(n)$, distinctions can be made on whether these inhomogeneities are on large scale (clustered) or small scale (evenly distributed with higher local differences). With the help of the radial Fourier projection $p_r(m)$ and/or Bessel projection $p_r(m_B)$ the radial distribution of inhomogeneities can be characterized. While the radial characterization is weaker than the azimuthal, it is also less important, since the radial intensity distribution is determined mainly by the diffraction pattern, which is again determined by the BSA size. The BSA size however is chosen as a compromise between thermal emittance and space charge induced emittance growth, and is therefore no degree of freedom in the emittance optimization.

Two-dimensional integral transforms have been studied but where dismissed due to complexity and limited use.

In the next step, the suggested parameters need to be tested for their influence on the emittance. There are two ways to do this, measurements and simulations. Measurements are probably the inferior option: on the one hand, because for a sufficient number of measurements with varying spot sizes (and thereby different diffraction patterns), a lot of accelerator run time needs to be invested. On the other hand, the spatial distribution of the laser intensity cannot be modified arbitrarily and variation is very limited for a fixed spot size. The possible small variations are probably not enough to clarify correlations between emittance and the characterization parameters. Especially relating the effects on the emittance to individual parameters will hardly be possible this way. Considering these limitations, it makes little sense to spend valuable beam time on this. Also, the measured emittance depends on

various other machine parameters, which were usually varied in past measurements, while the laser spot remained the same, so these are not useful here. Simulation, on the other hand, only requires a given laser intensity distribution to calculate the emittance at a certain point in the accelerator. By generating arbitrary intensity distribution it is possible to a certain degree, to specifically change individual characterization parameters, which allows systematic studies. At this point, another problem shows up. The ASTRA simulation software [25] used at PITZ can only simulate the emission of rotational symmetric distributions. This limitation makes the systematic testing of the azimuthal Fourier projections $p(n)$ and $p_c(n)$ impossible. As a first step of validation of the other characterization parameters it is possible, to generate and simulate rotational symmetric intensity distributions, preferably with $c_0(r)$ of the azimuthal Fourier transform of actual laser spots as a profile. Anyway, these studies have to be used with caution, since azimuthal asymmetries of the actual spots will have a significant impact on the emittance. Still, these simulations should provide good estimates at least.

Another important step on the way towards practical applications of the algorithm are high resolution measurements of the quantum efficiency of the photocathode. Details in the analysis of the laser spots, that are smaller than this resolution cannot have any relevance in further emittance studies. If high resolution measurements suggest, that small scale inhomogeneities of the quantum efficiency are negligible, interpolated data of rougher existing measurements can be used in practice. The inclusion of the quantum efficiency into the analysis is possible by simply multiplying the laser intensity within the AOI with the corresponding quantum efficiency data. The definition of the AOI based on the laser spots remains sensible, since the weighting of the flanks is not changed. There is no reason to assume that the inhomogeneities of the quantum efficiency are subject to patterns like the diffraction patterns of the laser images, so the introduction of further characterization parameters or analyses will probably not be necessary.

Despite the limited options for systematic studies of the individual parameters, it is very likely, that -with the help of the algorithm and the quantification of the laser spot characteristics- the operation crew can establish guidelines whereby the electron beam emittance can be minimized. It is not clear yet, if the application of these rules will still require the program. If so, the application of the program at FLASH and XFEL are imaginable, since both have a laser imaging system similar to PITZ. Though, a longer distance between BSA and lens system results in smaller diffraction patterns [26], which may require minor adaptations, e.g. the preference of Λ over ϱ.

Bibliography

[1] P. Schmüser, M. Dohlus, and J. Rossbach. *Ultraviolet and Soft X-Ray Free-Electron Lasers.* Springer Berlin Heidelberg, 9th edition, 2008.

[2] M. Reiser. *Theory and Design of Charged Particle Beams.* John Wiley and Sons, 2nd edition, 2008.

[3] S. Lederer et al. Investigations on the Thermal Emittance of Cs_2Te Photo-cathodes at PITZ. In *Proceedings of the 29th International FEL Conference*, Novosibirsk, Russia, 2007.

[4] K. Flöttmann. Note on the Thermal Emittance of Electrons Emitted by Cesium Telluride Photo Cathodes. TESLA FEL-Report 1997-01, DESY, 1997.

[5] R. A. Powell, W. Spicer, G. Fisher, and P. Gregory. Photoemission studies of cesium telluride. *Phys. Rev. B*, 5(8):3987–3995, October 1973.

[6] Y. Ivanisenko. *Investigation of Slice Emittance Using an Energy-chirped Electron Beam in a Dispersive Section for Photo Injector Characterization at PITZ.* PhD thesis, Universität Hamburg, 2012.

[7] M. Quattromini, L. Giannessi, and C. Ronsivalle. Emittance dilution due to 3D perturbations in RF-photoinjectors. In *Proceedings of EPAC 2004, Lucerne, Switzerland*, pages 2607–2609, 2004.

[8] M. Quattromini, L. Giannessi, and C. Ronsivalle. Spectral Analysis of Charge Emission Spatial Inhomogeneities and Emittance Dilution in RF Guns. In *Proceedings of the 2004 FEL Conference*, pages 411–414, 2004.

[9] V. Fusco, M. Ferrario, and C. Ronsivalle. Spatial Correlation for Laser Beam Quality Evaluation. Technical Report SPARC-EBD-07/007, INFN/LNF, 2007.

[10] M. Hänel. *Experimental Investigations on the Influence of the Photocathode Laser Pulse Parameters on the Electron Bunch Quality in an RF - Photoelectron Source.* PhD thesis, Universität Hamburg, 2010.

[11] S. Lederer et al. XPS Investigations on Cs_2Te photocathodes of FLASH and PITZ. In *Proceedings of PAC09*, Vancouver, BC, Canada, 2009.

[12] V. Miltchev. *Investigations on the transverse phase space at a photo injector for minimized emittance.* PhD thesis, Humboldt-Universität zu Berlin, 2006.

[13] G. Asova. *Tomography of the electron transverse phase space at PITZ.* PhD thesis, INRNE, BAS, Sofia, Bulgaria, 2012.

[14] I. Will and G. Klemz. Generation of flat-top picosecond pulses by coherent pulse stackingin a multicrystal birefringent filter. *Opt. Express*, 16(19):14922–14937, Sep 2008.

[15] S. Weisse et al. TINE Video System: Proceedings on Redesign. In *Proc. of ICALEPCS 2009*, 2009.

[16] M. Groß and G. Klemz. Diffraction Effects in the Laser Beam Line at PITZ. PITZ Collaboration Meeting, October 2011, DESY.

[17] M. Groß. private communication. 2012.

[18] M. Groß. Laser Pointing Stability: Measurement Results. PITZ Physics Seminar, August 2011, DESY.

[19] S. De Silvestri, P. Laporta, V. Magni, and O. Svelto. Solid-state laser unstable resonators with tapered reflectivity mirrors: the super-gaussian approach. *Quantum Electronics, IEEE Journal of*, 24(6):1172 –1177, jun 1988.

[20] R. J. Barlow. *Statistics - A Guide to the Use of Statistical Methods in the Physical Sciences.* John Wiley and Sons, 1989.

[21] V. Fusco. private communication. 2012.

[22] G. N. Watson. *A treatise on the theory of the Bessel functions.* Cambridge University Press, 2nd edition, 1922.

[23] G. B. Arfken and H. Weber. *Mathematical methods for physicists.* Harcourt/Academic Press, 5th edition, 2001.

[24] J. Lundgren. ZEROBESS. `http://www.mathworks.com/matlabcentral/fileexchange/26639-zerobess`, 2011.

[25] K. Flöttmann. A space charge tracking code - ASTRA. `http://www.desy.de/~mpyflo/`.

[26] G. Klemz. private communication. 2013.

Eigenständigkeitserklärung

Hiermit versichere ich, dass ich die vorliegende Arbeit selbständig verfasst und keine anderen als die angegebenen Quellen und Hilfsmittel verwendet habe.

Berlin, den 20.03.2013   Roman Martin